Faithful effective-one-body waveform of small-mass-ratio coalescing black hole binaries: The eccentric, nonspinning case

Simone Albanesi,[1,2] Sebastiano Bernuzzi,[3] Thibault Damour,[4] Alessandro Nagar,[1,4] and Andrea Placidi[5,6,7]

[1]*INFN sezione di Torino, Torino, 10125, Italy*
[2]*Dipartimento di Fisica, Università di Torino, Torino, 10125, Italy*
[3]*Theoretisch-Physikalisches Institut, Friedrich-Schiller-Universität Jena, 07743, Jena, Germany*
[4]*Institut des Hautes Etudes Scientifiques, 35 Route de Chartres, Bures-sur-Yvette, 91440, France*
[5]*Dipartimento di Fisica e Geologia, Università di Perugia, Via A. Pascoli, 06123 Perugia, Italia*
[6]*Niels Bohr Institute, Copenhagen University, Blegdamsvej 17, DK-2100 Copenhagen Ø, Denmark*
[7]*Galileo Galilei Institute for Theoretical Physics, Largo Enrico Fermi, 2, 50125 Firenze, Italy*

(Received 4 June 2023; accepted 15 September 2023; published 17 October 2023)

We present a new effective-one-body (EOB) waveform for eccentric, nonspinning binaries in the extreme mass ratio limit, with initial eccentricities up to 0.95. The EOB analytical waveform, that includes noncircular corrections up to second post-Newtonian order, is completed by a phenomenological ringdown model that is informed by Regge-Wheeler-Zerilli (RWZ) type waveforms generated by a point-particle source. This model notably includes the beating between positive and negative frequency quasinormal modes (QNMs). We analyze various prescriptions to faithfully complete the analytical EOB waveform in the transition from plunge to merger. In particular, we systematically explore the effect of: (i) the generic Newtonian prefactor; (ii) next-to-quasicircular (NQC) corrections to amplitude and phase; (iii) the point where NQC corrections are determined; (iv) the ringdown attachment point. This yields EOB/RWZ quadrupolar phase differences through merger and ringdown $\lesssim 0.01$ rad for the quasicircular case and $\lesssim 0.05$ rad for the eccentric case. Higher modes are also modeled up to the $\ell = m = 5$ multipole. We finally discuss the excitation of the QNMs and present a heuristic model to motivate it in correlation with the presence of a point-particle source.

DOI: 10.1103/PhysRevD.108.084037

I. INTRODUCTION

The gravitational waves (GWs) that have been detected by the interferometers of the LIGO-Virgo-KAGRA collaboration [1–4] were generated by the coalescence of comparable mass binaries, mainly black hole binaries. Since accurate waveform models are required to analyze these signals without biases, many efforts have been devoted to build accurate and fast semianalytical models using different approaches. However, there are no analytical solutions of the Einstein field equations for the merger of the two objects, even if one considers only vacuum-solutions. Therefore, all the currently available semianalytical models that are able to provide waveforms for the inspiral, plunge merger and ringdown of the binaries are informed/calibrated using numerical results.

One of the semianalytical approaches that has been proved to be accurate and fast enough to perform parameter estimations [2–6] is the effective-one-body (EOB) model [7–11]. While the pure analytical EOB approach can be used to faithfully describe only the inspiral of compact binaries, it is possible to use numerical data to extend the model and describe also the merger and ringdown of the system [12,13]. Notably, EOB models can be improved and completed using both numerical results from comparable mass binaries and from the extreme-mass-ratio regime. This is linked to the fact that, given a system of two compact objects with masses m_1 and m_2, the EOB metric is a ν-deformation of a black hole solution, being $\nu = \mu/M$ the symmetric mass ratio and $\mu = m_1 m_2/(m_1 + m_2)$ and $M = m_1 + m_2$ the reduced and total mass of the binary, respectively. Consequently, the test-mass limit is smoothly connected to the comparable mass case. The dawn of what is nowadays the established gravitational waveform modeling via the EOB approach informed by numerical simulations can be traced back to two seminal papers, one by Buonanno, Cook and Pretorius [12], and the other by Damour and Nagar [13]. The former used the pioneering numerical relativity (NR) simulation of equal mass, nonspinning black hole binary [14], while the latter considered the quasicircular inspiral and plunge of a nonspinning test particle in a Schwarzschild black hole [15]. Since the test-mass limit is a controlled theoretical laboratory to test prescriptions to use also in the comparable mass case, it has been explored in many EOB works, see e.g. Refs. [13,15–20] Moreover, this limit is also interesting by itself, since the space-based mission

LISA [21] will be able to detect extreme-mass-ratio-inspirals (EMRIs) [22,23]. However, to model these astrophysical systems, an accurate description of the dynamics is needed. The gravitational self-force (GSF) community has devoted many efforts in tackling this problem [24–27], with techniques and results that are beyond the scope of this work. We just mention that the EOB approach was recently shown to accurately describe the dynamics of GSF-evolved EMRIs in the quasicircular case [28,29] once informed by GSF-results [30–35]. In this work we focus instead on the EOB prescription to compute the waveform at infinity for a nonspinning test particle plunging in a Schwarzschild black hole after an eccentric inspiral. The numerical data used to build the ringdown model, and thus complete the EOB waveform, are obtained solving numerically the Regge-Wheeler and Zerilli (RWZ) equations [36–39] using the time domain code RWZhyp [16,40,41]. We argue that a description based exclusively on quasinormal modes (QNMs) cannot be used to describe the ringdown waveform starting from the peak of the amplitude. We rather use a modified version of the phenomenologically agnostic ringdown model presented in Ref. [42]. We model the (2,2) multipole and also all the $m > 0$ higher modes up to $\ell = 4$, plus the (5,5) mode. The complete waveform obtained is, to our knowledge, the most accurate EOB waveform for a nonspinning test particle on quasicircular inspirals in Schwarzschild spacetime, and also generalize well to highly eccentric dynamics. To conclude, we also discuss how the QNMs build-up during the last stages of the evolution of the binary. Among other phenomenological results, we find that the overtones are excited before the fundamental QNM, confirming the qualitative arguments presented in Ref. [13].

The paper is structured as follows. In Sec. II we discuss how we compute the approximate dynamics of the particle, the numerical RWZ waveform and the modeling of the ringdown. In Sec. III we discuss the inspiral waveform and how we match it to the ringdown model using the NQC corrections. The complete EOB waveform obtained is then compared to the original numerical results in Sec. IV. In Sec. V we further analyze the QNMs contributions in the postpeak waveform and we revisit the matching of the ringdown model using an extended time interval. The build up of the QNMs excitation is discussed in Sec. VI. The rescaled phase-space variables that we use in this work are related to the physical ones by $t = T/(GM)$, $r = R/(GM)$, $p_r = P_R/\mu$, and $p_\varphi = P_\varphi/(\mu GM)$. We will also use geometric units $G = c = 1$.

II. FROM ECCENTRIC INSPIRAL TO PLUNGE, MERGER, AND RINGDOWN

The radiation-reaction-driven transition from eccentric inspiral to plunge, merger, and ringdown in the large mass ratio limit and the emitted gravitational waveform (computed using black-hole perturbation theory) were first discussed in Ref. [43] and then more in extenso in Sec. V B of Ref. [20] (notably also allowing the central black hole to spin). In the same Sec. V B of Ref. [20] we also presented a (preliminary) complete effective-one-body-based waveform model including merger and ringdown for the $\ell = m = 2$ mode. In this section we build upon Ref. [20] and complement the description of the dynamics and waveform phenomenology described there. In particular, we: (i) present a precise description of the transition from inspiral to plunge and its dependence on the eccentricity; (ii) explicitly present an analytical description of the postpeak waveform, that improves the one presented in Ref. [20] and that is crucial (as we will see) to construct a complete EOB waveform, that is the main goal of Sec. III below. Here we focus on the nonspinning case only, while the spinning case will be discussed elsewhere. The radiation-reaction-driven relative dynamics is obtained solving Hamilton's equations in the presence of driving forces, that read

$$\dot{r} = \frac{A}{\hat{H}} p_{r_*}, \tag{1a}$$

$$\dot{\varphi} = \frac{A}{\hat{H}} \frac{p_\varphi}{r^2} \equiv \Omega, \tag{1b}$$

$$\dot{p}_{r_*} = A\hat{\mathcal{F}}_r - \frac{A}{r^2\hat{H}}\left[p_\varphi^2\left(\frac{3}{r^2} - \frac{1}{r}\right) + 1\right], \tag{1c}$$

$$\dot{p}_\varphi = \hat{\mathcal{F}}_\varphi, \tag{1d}$$

where $A = 1–2/r$ is the metric Schwarzschild potential, p_{r_*} is the conjugate momentum of the tortoise coordinate $r_* = r + 2\log(r/2 - 1)$, and $\hat{H}$ is the μ-normalized Hamiltonian of a test particle on Schwarzschild,

$$\hat{H} = \sqrt{A(r)\left(1 + \frac{p_\varphi^2}{r^2}\right) + p_{r_*}^2}. \tag{2}$$

The explicit form of $\hat{\mathcal{F}}_\varphi$ and $\hat{\mathcal{F}}_r$ can be found in Refs. [20,43].

Let us also remind that, as in Ref. [20], we define the eccentricity e and the semilatus rectum p in terms of the two radial turning points, the periastron r_- and the apastron r_+,

$$e = \frac{r_+ - r_-}{r_+ + r_-} \tag{3}$$

$$p = \frac{2r_+r_-}{r_+ + r_-}. \tag{4}$$

Note that this definition yields $r_\pm = p/(1 \mp e)$. The link between (e, p) and the energy and angular momentum, $(\hat{E}, p_\varphi)$, is simply obtained by solving the energy condition

$\hat{E} = \hat{H}|_{p_{r_*}=0}$ evaluated at the two radial turning points. In order to have stable orbits, the semilatus rectum must satisfy the condition $p \geq p_s = 6 + 2e$, where p_s is known as the separatrix and reduces to the last stable orbit (LSO) in the quasicircular case. In this work we will consider configurations with initial eccentricities up to $e_0 = 0.95$ and semilatera recta such that the particle undergoes at least a few radial orbits before plunging in the black hole. The simulations considered in this work are listed in Table I. The dynamics is always started at the apastron, so that the initial radial momentum is zero. Note that we chose (e_0, p_0) in order to have a clear geometrical intuition of the orbit, but we immediately convert (e_0, p_0) in energy and angular momentum so that we have all the needed initial values to compute the dynamics from Hamilton's equations. Note that since the dynamics is not conservative, e and p are not constants of motion and are not defined through the whole evolution of the binary. Indeed, after the separatrix-crossing time $t_{\rm sep}$, i.e., the time at which the condition $p(t) = p_s(t)$ is met, the periastron is no longer defined and thus neither the eccentricity and the semilatus rectum. Since in the next sections we will focus on the last part of the dynamics, we will often use $e_{\rm sep} = e(t_{\rm sep})$ to refer to a certain simulation, rather than e_0. Note however that this is only for labeling purposes, the eccentricity $e(t)$ is not actually used anywhere during the evolution.

TABLE I. Configurations considered and relevant quantities at merger time, defined as the peak of the orbital frequency. From left to right: initial semilatus rectum, initial eccentricity, eccentricity at the separatrix-crossing time, time difference between the peak of the orbital frequency and the peak of the quadrupolar amplitude, energy, angular momentum and quadrupolar amplitude at the peak of the orbital frequency (that corresponds to the light-ring crossing).

Number	p_0	e_0	$e_{\rm sep}$	$t^{\rm peak}_{\Omega_{\rm orb}} - t^{\rm peak}_{A_{22}}$	$\hat{E}^{\rm LR}$	$p^{\rm LR}_\varphi$	$A^{\rm LR}_{22}$
1	7.0	0.00	0.000	2.559	0.9422	3.4574	0.2928
2	7.3	0.05	0.061	2.585	0.9424	3.4598	0.2932
3	7.0	0.10	0.113	2.657	0.9429	3.4668	0.2942
4	8.0	0.15	0.141	2.708	0.9433	3.4717	0.2950
5	7.5	0.20	0.201	2.856	0.9444	3.4855	0.2970
6	8.0	0.25	0.229	2.925	0.9450	3.4932	0.2981
7	8.0	0.30	0.276	3.080	0.9462	3.5081	0.3003
8	8.0	0.35	0.321	3.240	0.9476	3.5243	0.3027
9	7.5	0.40	0.393	3.538	0.9503	3.5544	0.3070
10	8.0	0.45	0.415	3.651	0.9513	3.5644	0.3085
11	7.7	0.50	0.482	4.004	0.9545	3.5984	0.3133
12	8.0	0.55	0.514	4.189	0.9563	3.6159	0.3158
13	8.0	0.60	0.563	4.479	0.9592	3.6447	0.3199
14	8.0	0.65	0.615	4.839	0.9625	3.6768	0.3245
15	8.0	0.70	0.670	5.298	0.9665	3.7142	0.3298
16	8.0	0.75	0.728	5.877	0.9710	3.7554	0.3359
17	8.0	0.80	0.778	6.284	0.9751	3.7912	0.3408
18	8.2	0.85	0.818	6.628	0.9784	3.8202	0.3451
19	8.3	0.90	0.869	7.497	0.9839	3.8684	0.3523
20	8.5	0.95	0.904	8.160	0.9878	3.9004	0.3566

In our conventions, the strain waveform is decomposed in multipoles as

$$h_+ - \mathrm{i}h_\times = D_L^{-1} \sum_{\ell=2}^{\infty} \sum_{m=-\ell}^{\ell} h_{\ell m} {}_{-2}Y_{\ell m}(\Theta, \Phi), \tag{5}$$

where D_L is the luminosity distance and ${}_{-2}Y_{\ell m}(\Theta, \Phi)$ are the spin-weighted spherical harmonics with weight $s = -2$. The numerical waveform at linear order in ν is obtained solving the Regge-Wheeler and Zerilli [36,37] equations

$$\partial_t^2 \Psi^{(\mathrm{o/e})}_{\ell m} - \partial_{r_*}^2 \Psi^{(\mathrm{o/e})}_{\ell m} + V^{(\mathrm{o/e})}_\ell \Psi^{(\mathrm{o/e})}_{\ell m} = S^{(\mathrm{o/e})}_{\ell m}, \tag{6}$$

where the superscripts (e) and (o) distinguish respectively even parity ($\ell + m$ even) and odd parity ($\ell + m$ odd) solutions and the corresponding potentials $V^{(\mathrm{o/e})}_\ell$ and sources $S^{(\mathrm{o/e})}_{\ell m}$. The $\Psi^{(\mathrm{o/e})}_{\ell m}(t)$, are related to the waveform multipoles of Eq. (5) as $\Psi^{(\mathrm{o/e})}_{\ell m}(t) = h_{\ell m}(t)/\sqrt{(\ell+2)(\ell+1)\ell(\ell-1)}$. We solve the RWZ equations using the time domain code RWZhyp [16,40,41].

A. Transition from eccentric inspiral to plunge

Let us discuss the main qualitative features of the transition from an eccentric inspiral to plunge and merger. To do so pedagogically, let us first remind the reader how this transition occurs in the quasicircular case. The (quasi)circular inspiral is approximately representable as a sequence of circular orbits. The radius r_c of each circular orbit (with $r > r_{\rm LSO}$) corresponds to the local minimum of the radial potential

$$W = \left(1 - \frac{2}{r}\right)\left(1 + \frac{p_\varphi^2}{r^2}\right), \tag{7}$$

i.e., defined by the condition $\partial_r(W)|_{r=r_c} = 0$, and its energy is $\hat{E} = \sqrt{W_{\rm min}}$, where $W(r_c) = W_{\rm min}$ Since radiation reaction eliminates angular momentum from the system, the potential W is modified during the evolution, until the local maximum and minimum fuse together in an inflection point at the last stable orbit (LSO), $r = r_{\rm LSO} = 6$, where $\partial_r W = \partial_r^2 W = 0$ and $p_\varphi^{\rm LSO} = 2\sqrt{3}$. The evolution of the potential and the energy for the quasicircular case up to $t_{\rm LSO}$ are shown in the first panel of Fig. 1. We highlight in blue the potential at $t_{\rm LSO}$, after which the particle plunges into the black hole.

Eccentric orbits occur when $\sqrt{W_{\rm min}} < \hat{E} \leq \sqrt{W_{\rm max}}$, and the radial motion is confined between the two turning points, apastron and periastron. Since angular momentum is not conserved due to gravitational wave emission, the potential changes in time until a moment when

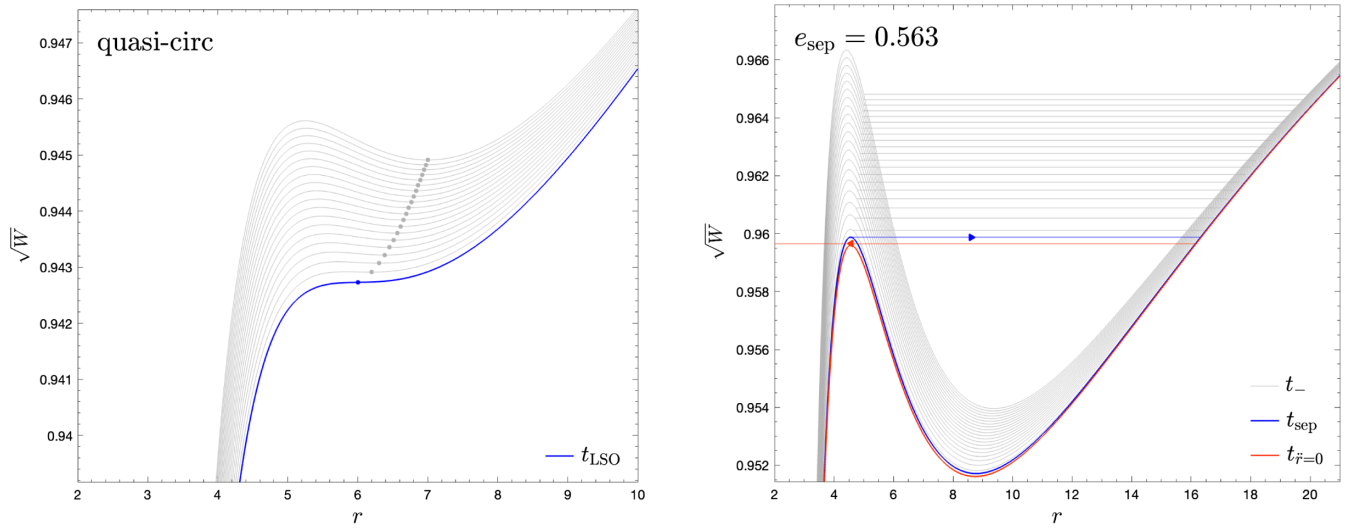

FIG. 1. Left panel: the evolution of radial effective potential W, Eq. (7), along the transition from quasicircular inspiral up to the last stable orbit. The LSO potential is highlighted, while the minima (identified by visible markers) indicate the radius and energy of the particle. Right panel: eccentric case with initial eccentricity $e_0 = 0.6$ ($e_{\rm sep} = 0.563$). We show a sequence of potentials W (that change due to radiation reaction) and corresponding energies of the particle at the periastron (horizontal line, gray) during the bound motion of the inspiral. The quantities at the separatrix crossing are shown in blue, while the red lines correspond to the beginning of the plunge. Note that in this case one has $V_{\rm max} \lesssim E$. The horizontal arrows mark the radial location (and energy) of the particle along the orbit at $t = t_{\rm sep}$ and at $t = t_{\ddot{r}=0}$. Note that the arrows point toward the corrisponding direction of the radial motion, outgoing for $t = t_{\rm sep}$ and ingoing for $t = t_{\ddot{r}=0}$. This latter point can be considered a *missed* periastron and practically marks the beginning of the plunge.

$\hat{E} = \sqrt{W_{\rm max}}$. After this, the periastron no longer exists (and thus e and p are no longer defined). As the energy of the particle approaches the maximum of the potential, the radial velocity eventually reaches a local minimum $|\dot{r}|_{\rm min} \neq 0$ and the radial acceleration $\ddot{r}$ changes sign, forcing the particle to plunge into the black hole. We identify this time, $t_{\ddot{r}=0}$, as the beginning of the plunge. The evolution of the potential for a configuration with initial eccentricity $e_0 = 0.6$ is shown in the right panel of Fig. 1. In this example the particle undergoes many eccentric orbits, then it crosses the separatrix while moving away from the central black hole (blue marker). The particle then reaches the apastron, inverts the motion and eventually crosses the potential barrier at approximately $t_{\ddot{r}=0}$ (red marker), where the plunge starts. We also show the corresponding trajectory, the radial evolution and the corresponding waveform in Fig. 2. Looking at $r(t)$, it is clear that $t_{\ddot{r}=0}$ can be though as a *missed* periastron. In the same figure, we also show the quasicircular configuration and another eccentric case with higher initial eccentricity, $e_0 = 0.9$. Note that in this highly eccentric case there is a long-lasting circular whirl around the plunge, while in the previous case the whirl around $t_{\ddot{r}=0}$ was much shorter. This phenomenology is linked to when $t_{\rm sep}$ occurs. In the $e = 0.9$ case, the particle crosses the separatrix slightly before the plunge and thus the energy at $t_{\ddot{r}=0}$ is quite close to the maximum of the radial potential. As a consequence, the particle undergoes a long-lasting quasicircular whirl.[1] In the case with $e_0 = 0.6$, the separatrix crossing occurs slightly after the last periastron passage and thus the effect of the radiation reaction during the last radial orbit increases the difference between the energy and the maximum of the radial potential at the beginning of the plunge (in this case we have $\hat{E} - \sqrt{W_{\rm max}} \simeq 5 \times 10^{-5}$, while in the more eccentric one we had 2×10^{-6}). Therefore, in our $e_0 = 0.6$ case the particle has a shorter quasicircular whirl before the plunge with respect to our $e_0 = 0.9$ case. For similar reasons, the configuration with $e_0 = 0.5$ has a longer whirl at $t_{\ddot{r}=0}$ than the configuration with $e_0 = 0.8$. We thus confirm that the length of the quasicircular behavior occurring before the plunge does not simply depend on the value of eccentricity.

Since the beginning of the plunge is a *missed* periastron and the eccentricity is a slowly varying quantity, the radius that marks the beginning of the plunge can be approximated as $r_{\rm plunge} \simeq (6 + 2e_{\rm sep})/(1 + e_{\rm sep})$ and it is always smaller than $r = 6$. The net result of this, together with the considerations above, is that the plunge is more adiabatic in the presence of eccentricity than in the quasicircular case. This is made quantitative in Fig. 3, that depicts the adiabatic estimator $\dot{\Omega}/\Omega^2$ as function of Ω for some

[1]We recall that if the energy is close to the peak of the radial potential, the orbits show a zoom-whirl behavior, see, e.g., Ref. [44].

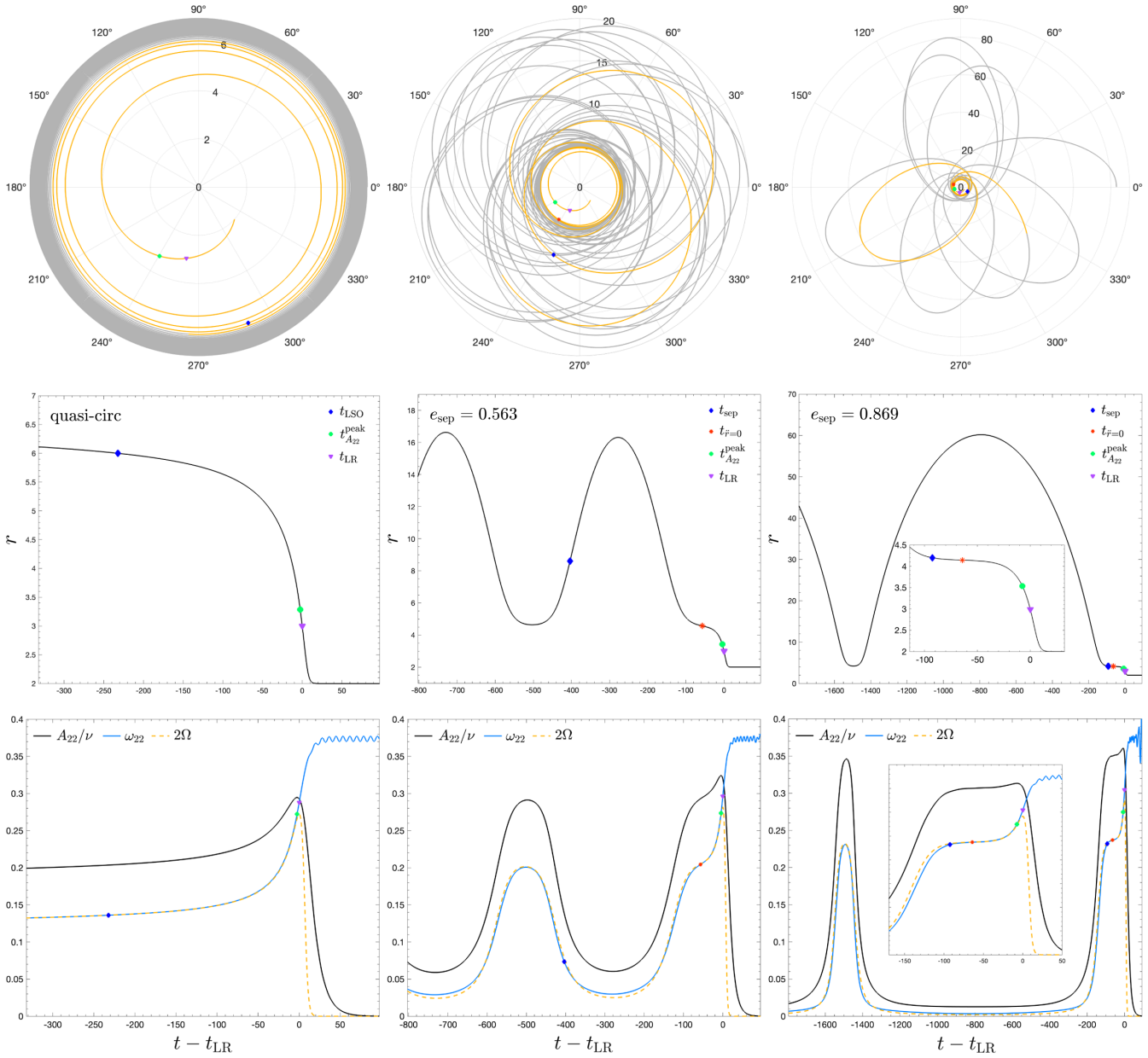

FIG. 2. Top row: trajectories for the three configurations with initial eccentricity $e_0 = \{0, 0.6, 0.9\}$. We highlight in orange the portions that correspond to the parts shown in the lower panels. In all the cases we mark the separatrix crossing with a blue diamond (LSO in the quasicircular case), the peak of the quadrupolar amplitude $t_{A_{22}}^{\rm peak}$ with a green circle, and the light-ring crossing time $t_{\rm LR}$ with a purple triangle. In the eccentric case we also highlight the inflection point of the radius that marks the end of the last radial orbit, $t_{\dot{r}=0}$, with a red star. Middle row: radius versus time, same markers as above. Bottom row: corresponding amplitude (black) and frequency (blue) of the quadrupolar waveforms. We also show the orbital frequency (dashed orange).

relevant configurations. For each dataset, the horizontal axis is restricted between $\Omega_{\dot{r}=0}$ and $\Omega_{\rm pk}$, that corresponds respectively to the orbital frequency at the start of the plunge and at the light-ring crossing.

B. Waveform phenomenology

The features of the dynamics that we have just discussed clearly reflect on the waveform phenomenology, as shown by the Zerilli (2,2) waveforms reported in the bottom row of Fig. 2; the amplitude is shown in black, the frequency in blue. The latter is also compared with the orbital frequency, Ω, shown in dashed orange. While in the circular case 2Ω is a remarkably good approximation of the waveform frequency ω_{22}, in the two eccentric cases the noncircular effects increase the differences between these two quantities during the inspiral. However, note that $\omega_{22} \simeq 2\Omega$ holds also during the plunge for the two eccentric cases, up to the time of the quadrupolar amplitude peak,

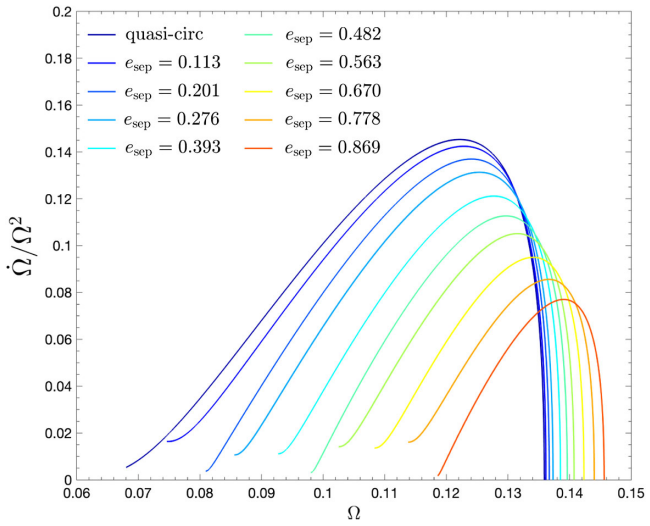

FIG. 3. Measure of adiabaticity, $\dot{\Omega}/\Omega^2$, for the quasicircular case and different eccentric configurations. The horizontal axis is restricted between $\Omega_{\dot{r}=0}$ and $\Omega_{\rm pk}$.

$t^{\rm peak}_{A_{22}}$ (marked with a green circle), i.e., shortly before the light-ring crossing $t_{\rm LR}$ (marked with a purple triangle). This can be easily understood considering that the eccentric plunge is rather adiabatic.

In order to better highlight the properties of the waveform for different eccentricities, in Fig. 4 we plot the (2,2) mode of the waveforms for $e_0 \in [0, 0.9]$. As a consequence of the fact that in highly eccentric configurations the plunge starts at smaller radii, the amplitude grows as the eccentricity increases and the peaks become wider. Moreover, the peaks occur at earlier times with respect to the light-ring crossing, as shown by the markers in the left panel. In the right panel of Fig. 4 we show the corresponding frequencies. After the light-ring crossing all the frequencies reach the fundamental positive quasinormal frequency of the Schwarzschild black hole. Notably, also the beating between the positive and negative fundamental quasinormal frequencies is not influenced by the nature of the perturbation. However, at later time the oscillations in the frequencies tend to grow for high eccentricity, but this is only an effect of the power-law tail that begins to dominate on the quasinormal-mode (QNM) contribution. We postpone the discussion of the tail to Sec. V D. We also highlight the inflection point of the frequencies using diamond markers. The location of this point is not strongly influenced by the eccentricity, but it is only slightly delayed with respect to the light-ring crossing. On the contrary, the location of the amplitude peak is strongly influenced by the eccentricity. This is a qualitative explanation of why the quasicircular ringdown model used in `TEOBResumS` is able to correctly reproduce the frequency of highly eccentric comparable mass configurations, but not their amplitudes (see the supplemental material of Ref. [5]).

C. Ringdown (postpeak) modeling

During the ringdown, a relevant contribution to the waveform is given by the QNMs. If this is the only contribution, then each multipole can be written as

$$\Psi^{(\rm o/e)}_{\ell m} = \sum_{n=1}^{\infty} (C^{+}_{\ell m n} e^{-\sigma^{+}_{\ell n}\tau} + C^{-}_{\ell m n} e^{-\sigma^{-}_{\ell n}\tau}), \tag{8}$$

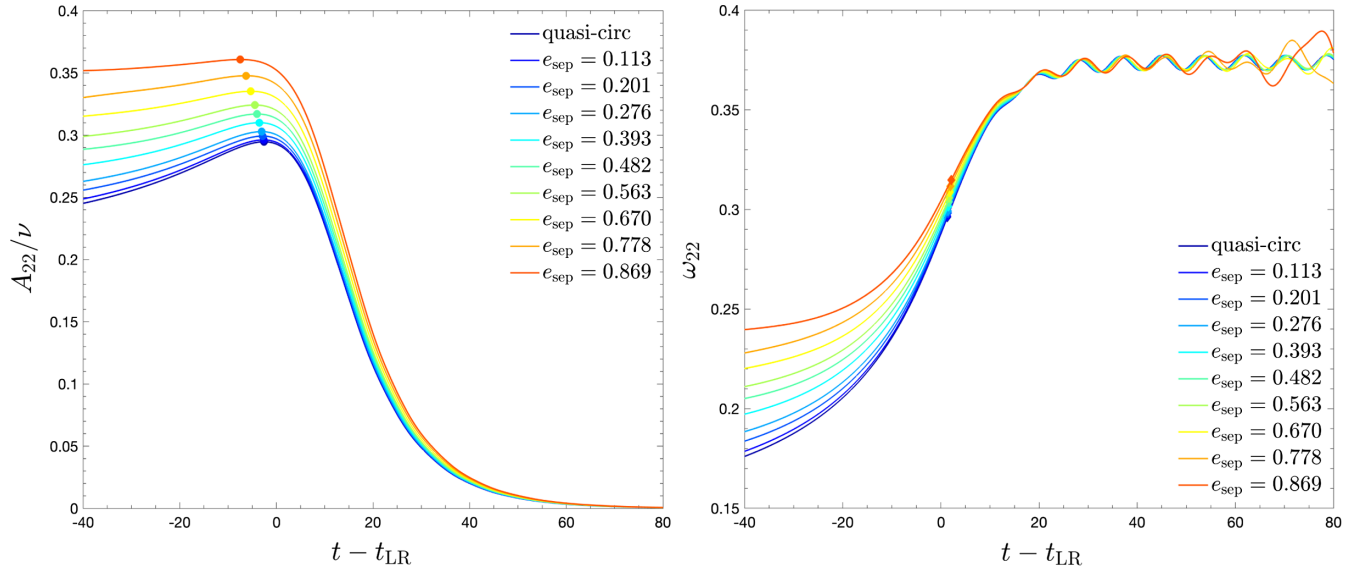

FIG. 4. Left panel: quadrupolar Zerilli amplitudes for different eccentricities, aligned with respect to the light-ring crossing. The dots mark the maxima of the amplitudes. Right panel: Zerilli frequencies for different eccentricities, always aligned using the light-ring crossing. The diamonds mark the inflection points of the frequencies.

where $\sigma^{\pm}_{\ell n} = \alpha_{\ell n} \pm i\omega_{\ell n}$ are the complex QNM frequencies, and the $C^{\pm}_{\ell mn}$ are complex constant coefficients.[2] While the latter depend on the type of the perturbation, the frequencies depend only on the mass of the Schwarzschild black hole. However, it has been shown that for comparable mass binaries the pure QNM description can be used only at later times [45]. In Sec. V we will argue that this is the case also for the postpeak waveform generated by a particle falling into a Schwarzschild black hole. Therefore, we comply to the phenomenological ideas introduced in Ref. [42], based on the idea of factorizing away the contribution of the fundamental quasinormal mode. We thus introduce the QNM-rescaled waveform

$$\bar{h}_{\ell m}(\tau) = e^{\sigma^{+}_{\ell 1}\tau + i\phi^{\rm peak}_{\ell m}} h^{\rm rng}_{\ell m}(\tau), \tag{9}$$

where $\tau = t - t^{\rm peak}_{A_{\ell m}}$, $\phi^{\rm peak}_{\ell m}$ is the value of the phase at the amplitude peak, and $h^{\rm rng}_{\ell m}$ is the ringdown waveform. The QNM-rescaled waveform $\bar{h}_{\ell m}(\tau)$ is then written using two templates for the amplitude and the phase, $\bar{h}(\tau) = A_{\bar{h}}(\tau)e^{i\phi_{\bar{h}}(\tau)}$. In Ref. [20], we pointed out that the original waveform template for the amplitude can become incorrect when the mass ratio is large. For this reason we introduced a different fitting function. Our templates thus read

$$A_{\bar{h}}(\tau) = \left(\frac{c^A_1}{1 + e^{-c^A_2\tau + c^A_3}} + c^A_4\right)^{\frac{1}{c^A_5}}, \tag{10}$$

$$\phi_{\bar{h}}(\tau) = -c^{\phi}_1 \ln\left(\frac{1 + c^{\phi}_3 e^{-c^{\phi}_2\tau} + c^{\phi}_4 e^{-2c^{\phi}_2\tau}}{1 + c^{\phi}_3 + c^{\phi}_4}\right), \tag{11}$$

where we have dropped the ℓm-indices for notation simplicity. The sets of parameters c^A and c^{ϕ} are constrained by requiring the continuity of the waveform at $\tau = 0$ with the inspiral waveform. Requiring the continuity of the amplitude, its first two time derivatives, and the frequency, we get

$$c^A_1 = \frac{c^A_5\alpha_1}{c^A_2}(A_{\rm peak})^{c^A_5} e^{-c^A_3}(1 + e^{c^A_3})^2, \tag{12}$$

$$c^A_4 = (A_{\rm peak})^{c^A_5} - \frac{c^A_1}{1 + e^{c^A_3}}, \tag{13}$$

$$c^A_5 = -\frac{\ddot{A}_{\rm peak}}{A_{\rm peak}\alpha_1^2} + \frac{c^A_2}{\alpha_1}\frac{e^{c^A_3} - 1}{1 + e^{c^A_3}}, \tag{14}$$

$$c^{\phi}_1 = \frac{1 + c^{\phi}_3 + c^{\phi}_4}{c^{\phi}_2(c^{\phi}_3 + 2c^{\phi}_4)}\Delta\omega_{\rm peak}, \tag{15}$$

where $\ddot{A}_{\rm peak}$ is the second time derivative of the amplitude evaluated at the peak, and $\Delta\omega_{\rm peak} \equiv \omega_1 - \omega_{\rm peak}$. Note that in previous works also the condition $c^{\phi}_2 = \Delta\alpha_{21} \equiv \alpha_2 - \alpha_1$ was imposed, here instead we leave c^{ϕ}_2 as a free parameter. The phase difference obtained with the constrained c^{ϕ}_2 using the damping times is shown in blue in the bottom-right panels of Fig. 5. The free c^{ϕ}_2 improves the phase, especially for $\ell = m$ modes.

With these templates we are able to fit the numerical postpeak waveform for each multipole and every eccentricity considered in this work. In the first row of Fig. 5 we show the primary fits for the (2,2), (2,1) and (3,3) modes for the quasicircular inspiral. The rescaled amplitude $A_{\bar{h}}$ and the rescaled phase $\phi_{\bar{h}}$ reach a plateau after $\simeq 2\tau_{\ell 1}$, where $\tau_{\ell 1} \equiv 1/\alpha_{\ell 1}$ is the QNM-damping time of the fundamental mode. This means that, at this stage of the evolution, the only relevant contribution to the waveform is given by the fundamental QNMs. Note that leaving c^{ϕ}_2 as a free parameter strongly improves the phase agreement for the (2,2) and (3,3) modes (cfr. red and blue lines in the phase difference of each plot), while it is not relevant for the (2,1) mode. Similar considerations hold for the configuration with $e_0 = 0.9$, that is shown in the bottom row of Fig. 5, and all the other eccentric configurations considered in this work.

D. Modeling the mode-mixing

The templates discussed above catch all the main features of the numerical waveform, except the mode-mixing generated by the negative-frequency QNMs. This effect can be already seen in the (2,2) mode, but become particularly relevant in the $m = 1$ modes, as shown for the (2,1) mode in Fig. 5. We will discuss this effect in more detail in Sec. V B, here we just mention that it can be simply included in the ringdown model doing the substitution

$$h^{\rm rng}_{\ell m}(\tau) \to h^{\rm rng}_{\ell m}(\tau)(1 + \hat{a}_{\ell m 1} e^{2i\omega_{\ell,1}\tau}\sigma(\tau;\tau^{\rm mm}_0)), \tag{16}$$

where $\hat{a}_{\ell m 1} = C^{-}_{\ell m 1}/C^{+}_{\ell m 1} \equiv \hat{A}_{\ell m 1} e^{i\theta_{\ell m 1}}$ and $\sigma(t;\tau^{\rm mm}_0) = 1/(1 + e^{-(\tau - \tau^{\rm mm}_0)})$ is a sigmoid that activates the mode-mixing correction. The $\hat{a}_{\ell m 1}$ coefficients can be extracted fitting the late ringdown frequency with a fundamental-QNM ansatz as outlined in Ref. [16]; in this work we will follow a more refined procedure that we will discuss in Sec. V B. Note that, despite the fact that $C^{\pm}_{\ell m 1}$ depend on the nature of the perturbation, the modulus of their ratio, $\hat{A}_{\ell m 1}$, does not seem to change with the eccentricity, as shown for example for the (2,2) mode in Fig. 4. The values of $\hat{A}_{\ell m 1}$ can be found in Table III, while the value of $\tau^{\rm mm}_0$ is

[2]Note that we denote the fundamental QNM mode with the index $n = 1$ so that the first overtone has index $n = 2$, while in other recent works the fundamental mode is denoted with 0.

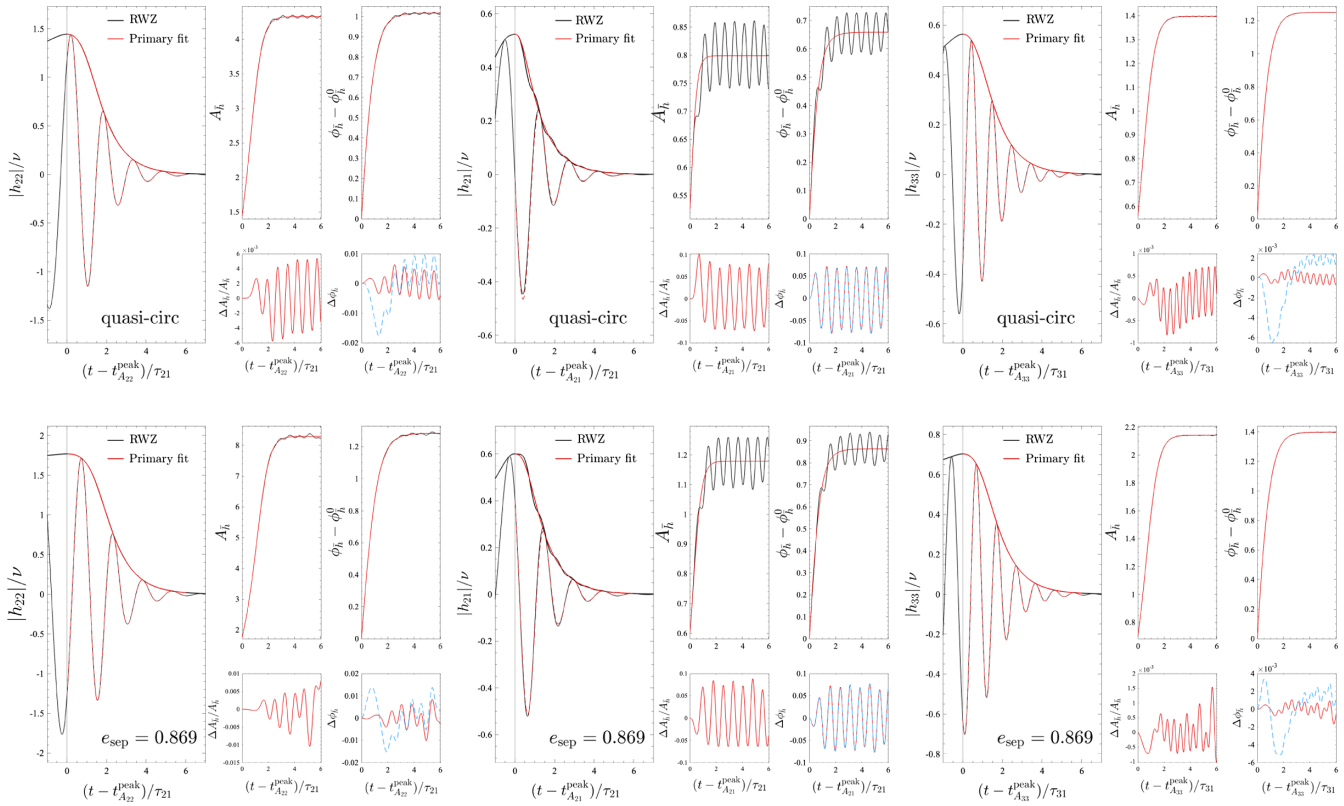

FIG. 5. Numerical waveform (black) and postpeak primary fits (red) for the (2,2), (2,1), and (3,3) modes for the quasicircular configuration (top row) and the configuration with $e_0 = 0.9$ (bottom row). We show the waveform $h_{\ell m}$ and its amplitude together with the QNM-rescaled amplitude $A_{\bar{h}}$ and phase $\phi_{\bar{h}}$. In the two small bottom panels we show the fit/numerical relative difference for the rescaled amplitude and the difference for the rescaled phase (red). Here $\phi^0_{\bar{h}}$ is the phase of $\bar{h}$ at $\tau = 0$, and $\tau_{\ell 1} = 1/\alpha_{\ell 1}$ is the QNM-damping time of the fundamental mode. We also show the RWZ/primary phase difference obtained imposing the condition $c^{\phi}_2 = \Delta\alpha_{21}$ in the primary fit (dashed blue).

chosen in order to introduce the oscillations in the analytical waveform only when they are also present in the numerical wave. For all the eccentricities, we use $\tau^{\rm mm}_0 = 25$ for the (2,2) multipole, $\tau^{\rm mm}_0 = 20$ for the $\ell = m$ higher modes, $\tau^{\rm mm}_0 = 8$ for (2,1), (3,2), (4,3), (4,2) and $t_0 = 3$ for (3,1) and (4,1).

E. Global fits

In Sec. II C and Sec. II D we have discussed a phenomenological model that can be used to faithfully describe the postpeak waveform. This model depends on different free parameters that are found fitting RWZ postpeak waveforms. However, in order to describe any eccentric case, we need to provide global fits of these parameters as function of some system-characterizing quantity. While the eccentricity would be an intuitive choice,[3] it is not a gauge invariant quantity and it is not defined through the whole evolution of the system. We thus use the quantity $b \equiv p_\varphi/\hat{E}$ evaluated at the peak of the orbital frequency (i.e., at the light-ring crossing) and shifted with the corresponding quasicircular value,

$$\hat{b}_{\Omega_{\rm pk}} = b_{\Omega_{\rm pk}} - b^{\rm QC}_{\Omega_{\rm pk}}, \tag{17}$$

where $b^{\rm QC}_{\Omega_{\rm pk}} = 3.6693$. Note that this parameter is gauge invariant since it is a combination of energy and angular momentum, and it vanishes in the quasicircular case. The latter feature is useful because we impose that the fits reduces to the exact values in the quasicircular case.

We thus proceed to perform the global fits for each multipole. Note that in our global fits we only use the simulations in Table I with odd identification number (#) (i.e. the simulations with "round" initial eccentricity), so that the eccentric simulations with even identification number can be though as a test set for the analytical model. We need to fit the free parameters of amplitude and phase templates, $\{c^A_2, c^A_3, c^{\phi}_2, c^{\phi}_3, c^{\phi}_4\}$, the quantities $\{A_{\rm peak}, \ddot{A}_{\rm peak}, \omega_{\rm peak}\}$ that are needed to compute the constrained parameters, and the phase θ_1 of the mode-mixing complex

[3]The eccentricity at the separatrix-crossing was used in the global fits performed in Ref. [20].

factor $\hat{a}_{\ell m1}$ (the modulus does not depends on the eccentricity). The primary fits are reported in Appendix C, and in particular in Tables V and VI. The fits for the mode-mixing are instead reported in Table IV.

III. EFFECTIVE-ONE-BODY WAVEFORM

A. Inspiral EOB waveform

The quasicircular EOB inspiral waveform for is obtained factorizing and resumming the post-Newtonian (PN) expanded multipoles [46],

$$h_{\ell m} = h_{\ell m}^{(N,\epsilon)_{\rm c}} \hat{h}_{\ell m}^{(\epsilon)_{\rm c}} = h_{\ell m}^{(N,\epsilon)_{\rm c}} \hat{S}^{(\epsilon)} \hat{h}_{\ell m}^{\rm tail} (\rho_{\ell m})^{\ell}, \tag{18}$$

where ϵ denotes the parity of the multipole, $h_{\ell m}^{(N,\epsilon)_{\rm c}}$ is the Newtonian circular contribution and $\hat{h}_{\ell m}^{(\epsilon)_{\rm c}}$ is the circular PN correction. The term $\hat{S}^{(\epsilon)}$ is the effective-source term, i.e., the energy if $\epsilon = 0$ or the Newtonian-normalized angular momentum if $\epsilon = 1$, $\hat{h}_{\ell m}^{\rm tail} = T_{\ell m} e^{i\delta_{\ell m}}$ is the tail factor and the $\rho_{\ell m}$ are the residual amplitude corrections.

The waveform (18) can be generalized to noncircular dynamics including corrections that are known up to 2PN [43,47–49]. In particular, Ref. [43] proposed to generalize the waveform of Eq. (18) generic orbits by simply replacing the Newtonian quasicircular prefactor with its general expression, i.e.,

$$h_{\ell m}^{(N,\epsilon)_{\rm c}} \to \hat{h}_{\ell m}^{(N,\epsilon)_{\rm c}} \hat{h}_{\ell m}^{(N,\epsilon)_{\rm nc}}. \tag{19}$$

For the (2,2) mode, the noncircular correction reads

$$\hat{h}_{22}^{(N,0)_{\rm nc}} = 1 - \frac{\ddot{r}}{2r\Omega^2} - \frac{\dot{r}^2}{2r^2\Omega^2} + \frac{2i\dot{r}}{r\Omega} + \frac{i\dot{\Omega}}{2\Omega^2}, \tag{20}$$

where r is the radius and Ω is the orbital frequency. The time derivatives in the generic Newtonian prefactor are computed using a 4th order centred stencil scheme, i.e., no PN-expanded equations of motion are used to compute them. While this correction is clearly crucial for eccentric inspirals, we will see that it is needed to improve the analytical/numerical agreement during the plunge also in the quasicircular case. The 2PN noncircular corrections to the Newtonian-factorized waveform provide a better analytical/numerical agreement for the phase during the inspiral [48,49], even if the main correction is given by the Newtonian term (19). In this work we will consider the noncircular hereditary term $\hat{h}_{22}^{\rm tail_{nc}}$ written in terms of $\dot{p}_{r_*}$ (see Eq. C1 of Ref. [48]) and the instantaneous corrections $\hat{h}_{22}^{\rm inst_{nc}}$ introduced in Ref. [49], so that the quadrupolar waveform reads

$$h_{22} = \hat{h}_{22}^{(N,\epsilon)_{\rm c}} \hat{h}_{22}^{(N,\epsilon)_{\rm nc}} \hat{h}_{22}^{(\epsilon)_{\rm c}} \hat{h}_{22}^{\rm inst_{nc}} \hat{h}_{22}^{\rm tail_{nc}}. \tag{21}$$

The 2PN noncircular corrections are switched-off at the beginning of the plunge using a sigmoid function, $\sigma(t) = 1/[1 + e^{-\alpha(t-t_{\rm plunge})}]$ with $\alpha = 0.2$, both for the eccentric and quasicircular cases. We do not consider 2PN noncircular corrections for the higher-modes. The relevance of these corrections in the quasicircular inspiral will be discussed in Sec. IV.

B. Next-to-quasicircular corrections

Even if the generic Newtonian prefactor of Eq. (20) is useful to improve the waveform during the plunge, we still need to correct the plunge waveform using numerical-informed correction known as next-to-quasicircular (NQC) corrections [13], especially for the higher modes. The complete EOB waveform is thus given by

$$h_{\ell m} = \theta(t_{\ell m}^{\rm match} - t) h_{\ell m}^{\rm inspl} \hat{h}_{\ell m}^{\rm NQC} + \theta(t - t_{\ell m}^{\rm match}) h_{\ell m}^{\rm rng}, \tag{22}$$

where $h_{\ell m}^{\rm inspl}$ is the inspiral EOB waveform discussed in Sec. III A, $h_{\ell m}^{\rm rng}$ is the ringdown discussed in Sec. II C, $\hat{h}_{\ell m}^{\rm NQC}$ is the NQC waveform correction, $\theta(x)$ is the Heaviside step function, and $t_{\ell m}^{\rm match}$ is the matching time. The NQC correction is written as

$$\hat{h}_{\ell m}^{\rm NQC} = \left(1 + \sum_{i=1}^{3} a_i^{\ell m} n_i\right) \exp\left(i \sum_{j=1}^{3} b_j^{\ell m} n_{j+3}\right), \tag{23}$$

where n_i are functions that are combinations of quantities negligible during the quasicircular inspiral but relevant during the plunge. To satisfy this requirement, it is natural to write them in terms of time derivatives of the radius or in terms of p_{r_*}. For all the higher modes we use the basis

$$n_1 = \frac{p_{r_*}^2}{r^2\Omega^2}, \tag{24a}$$

$$n_2 = \frac{\ddot{r}}{r\Omega^2}, \tag{24b}$$

$$n_3 = n_1 p_{r_*}^2, \tag{24c}$$

$$n_4 = \frac{p_{r_*}}{r\Omega}, \tag{24d}$$

$$n_5 = n_4 \Omega, \tag{24e}$$

$$n_6 = n_5 p_{r_*}^2. \tag{24f}$$

For the (2,2) mode, we use use the same n_i with $i \leq 4$, but we change $n_5 = n_4 r^2 \Omega^2$ and, consequently, $n_6 = n_5 p_{r_*}^2$. Note that in `TEOBResumS` only the first derivatives of A and ω are considered, so that n_3 and n_6 are not used. Moreover, in `TEOBResumS` the n_5 function for the higher modes is different than the one considered here.

The coefficients a_i and b_i are determined at a specific time $t^{\rm NQC}_{\ell m}$. If we consider $t^{\rm NQC}_{\ell m} > t^{\rm peak}_{A_{\ell m}}$, then they are determined solving the linear system

$$A^{\rm EOB}_{\ell m}(t^{\rm NQC}_{\ell m}) = A^{\rm rng}_{\ell m}(t^{\rm NQC}_{\ell m}), \tag{25a}$$

$$\dot{A}^{\rm EOB}_{\ell m}(t^{\rm NQC}_{\ell m}) = \dot{A}^{\rm rng}_{\ell m}(t^{\rm NQC}_{\ell m}), \tag{25b}$$

$$\ddot{A}^{\rm EOB}_{\ell m}(t^{\rm NQC}_{\ell m}) = \ddot{A}^{\rm rng}_{\ell m}(t^{\rm NQC}_{\ell m}), \tag{25c}$$

$$\omega^{\rm EOB}_{\ell m}(t^{\rm NQC}_{\ell m}) = \omega^{\rm rng}_{\ell m}(t^{\rm NQC}_{\ell m}), \tag{25d}$$

$$\dot{\omega}^{\rm EOB}_{\ell m}(t^{\rm NQC}_{\ell m}) = \dot{\omega}^{\rm rng}_{\ell m}(t^{\rm NQC}_{\ell m}), \tag{25e}$$

$$\ddot{\omega}^{\rm EOB}_{\ell m}(t^{\rm NQC}_{\ell m}) = \ddot{\omega}^{\rm rng}_{\ell m}(t^{\rm NQC}_{\ell m}), \tag{25f}$$

where on the left-hand side (lhs) the amplitude, frequency and corresponding time derivatives are computed from $h^{\rm inspl}_{\ell m}\hat{h}^{\rm NQC}_{\ell m}$, while on the right-hand side (rhs) they are computed from the ringdown model. If we want to use $t^{\rm NQC}_{\ell m} < t^{\rm peak}_{A_{\ell m}}$, on the rhs we have to consider quantities extracted from numerical data at $t^{\rm NQC}_{\ell m}$. Due to this reason, the choice $t^{\rm NQC}_{\ell m} > t^{\rm peak}_{A_{\ell m}}$ is, in principle, preferable since it reduces the number of numerical-informed parameters in the model. However, as we will see in more detail later, choosing $t^{\rm NQC}_{\ell m} < t^{\rm peak}_{A_{\ell m}}$ works better for the higher modes.

While the NQC correction is negligible during the quasicircular inspiral by construction, they are not negligible in eccentric inspirals since p_{r_*} is not small. For this reason we switch-off the NQC corrections during the eccentric inspiral using a sigmoid,

$$\hat{h}^{\rm NQC}_{\ell m} \to \hat{h}^{\rm NQC}_{\ell m}\frac{1}{1+e^{-\alpha^s(t-t_{\dot{r}=0})}}. \tag{26}$$

Given the discussion in Sec. II B, it is natural to center the sigmoid in $t_{\dot{r}=0}$ so that the NQC corrections are switched-on in a region where the motion is indeed quasicircular. Due to this choice, the relevance of the precise value of α^s is not crucial; in this work we will use $\alpha^s = 0.2$.

Finally, consider that to correctly evaluate the lhs of Eq. (25), an interpolation on a refined time grid is needed, see Appendix A for more details.

C. Matching point

The match of the plunge and ringdown waveform is performed at $t^{\rm NQC}_{\ell m}$ if $t^{\rm NQC}_{\ell m} > t^{\rm peak}_{A_{\ell m}}$, while it is performed at $t^{\rm peak}_{A_{\ell m}}$ if $t^{\rm NQC}_{\ell m} \leq t^{\rm peak}_{A_{\ell m}}$. The former prescription will be used for the (2,2) mode, while the latter will be used for the higher modes. In any case, in order to know the locations of $t^{\rm peak}_{A_{\ell m}}$, we need to link them to dynamical quantities. In the `TEOBResumS` model [50,51] and also in Ref. [20], the heuristic used to find the peak of the quadrupolar amplitude was

$$t^{\rm peak}_{A_{22}} = t^{\rm peak}_{\Omega_{\rm orb}} - \Delta t_{\rm NQC} - 2, \tag{27}$$

where $t^{\rm peak}_{\Omega_{\rm orb}}$ is the peak of the orbital frequency[4] and $\Delta t_{\rm NQC} = 1$. We keep $\Delta t_{\rm NQC}$ in the notation for continuity with previous works. The heuristic (27) gives satisfactory results in the quasicircular, since the exact value of $t^{\rm peak}_{A_{22}}$ extracted from the Zerilli waveform is $\Delta t^{\rm exact}_{\rm NQC} \simeq 0.559$. Most importably, Eq. (27) has been shown to be reliable also for quasicircular binaries of comparable mass. However, when dealing with highly eccentric binaries, the approximation $\Delta t_{\rm NQC} = 1$ is no longer valid and we thus perform a global fit as discussed in Sec. II E, finding

$$t^{\rm peak}_{A_{22}} = t^{\rm peak}_{\Omega_{\rm orb}} - \frac{2.559 + 7.574\hat{b}_{\Omega_{\rm pk}} - 18.830\hat{b}^2_{\Omega_{\rm pk}}}{1 - 2.160\hat{b}_{\Omega_{\rm pk}}}. \tag{28}$$

The peak amplitude of the other multipoles are delayed with respect to the quadrupolar one as

$$t^{\rm peak}_{A_{\ell m}} = t^{\rm peak}_{A_{22}} + \Delta t_{\ell m}, \tag{29}$$

with $\Delta t_{\ell m} > 0$ for all the higher modes. The values of $\Delta t_{\ell m}$ the quasicircular case, together with their global fits, are listed in Table II. The fact that $\Delta t_{\ell m}$ increases with m at fixed ℓ can be understood heuristically considering that all the m-modes have to reach the same final QNM frequency $\omega_{\ell,1}$ (modulo mode-mixing), but the waveform frequency during the inspiral is given by $\omega^{\rm inspl}_{\ell m} = m\Omega$ at leading order.

TABLE II. Time delays of the amplitude peaks $\Delta t_{\ell m}$ for the higher modes with respect to the peak of the (2,2) amplitude, see definition in Eq. (29). The global fitting template is $\Delta t_{\ell m} = (C^{\ell m}_{\rm QC} + C^{\ell m}_1\hat{b}_{\Omega_{\rm pk}} + C^{\ell m}_2\hat{b}^2_{\Omega_{\rm pk}})/(1 + D^{\ell m}_1\hat{b}_{\Omega_{\rm pk}})$, where $C^{\ell m}_{\rm QC}$ is the quasicircular value; see also discussion in Sec. II E.

(ℓ, m)	$C^{\ell m}_{\rm QC}$	$C^{\ell m}_1$	$C^{\ell m}_2$	$D^{\ell m}_1$
(2,1)	11.960	51.831	…	2.704
(3,3)	3.563	5.507	21.215	…
(3,2)	9.396	11.549	28.933	…
(3,1)	13.100	15.132	28.765	…
(4,4)	5.384	7.032	23.973	…
(4,3)	9.766	11.101	27.870	…
(4,2)	12.090	13.150	28.396	…
(4,1)	13.280	15.033	28.667	…
(5,5)	6.679	7.803	24.818	…

[4]Consider that for spinning binaries, $t^{\rm peak}_{\Omega_{\rm orb}}$ is the peak of the *pure* orbital frequency, that is computed without considering the spin-orbit terms.

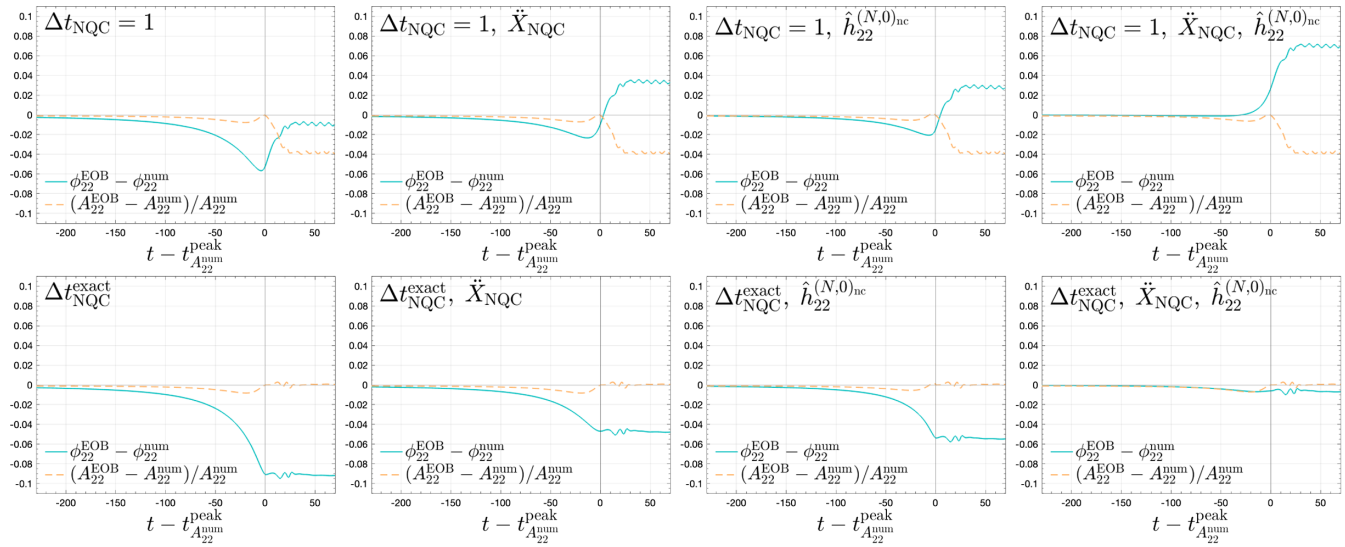

FIG. 6. Analytical/numerical differences for the amplitude and the phase (in radians) of the quadrupolar waveform for the quasicircular inspiral plunge in Schwarzschild. We consider different inspiral plunge and ringdown matching procedures. The differences are shown from the LSO crossing to $t^{\rm peak}_{A_{22}^{\rm num}} + 70$. In the upper panels we consider the matching time according to Eq. (27), while in the lower panels we use Eq. (28). Then, from left to right, we progressively improve the model considering the second time derivatives in the NQC base, $\ddot{A}_{22}$ and $\ddot{\omega}_{22}$, and then the Newtonian noncircular correction, $\hat{h}^{(N,0)_{\rm nc}}_{\ell m}$. The rightmost lower panel shows the differences for the state-of-the-art model.

Therefore, the modes with small m will need more time to reach the final frequency $\omega_{\ell,1}$.

We also point out that the mode-mixing becomes more relevant in low-m higher modes (see, e.g., Sec. V B), so that the position of the amplitude peak for the higher modes can be contaminated by the mode-mixing. Once that the location of the amplitude peak is known, we can proceed to match, mode by mode, the inspiral waveform to the ringdown model. From a computational point of view, the matching is performed on a time grid that is finer than the one used to solve the dynamics, see Appendix A for details.

IV. PROBING THE EFFECTIVE ONE BODY ANALYTICAL WAVEFORM

A. Quasicircular case

We start by analyzing in detail the quasicircular case, testing the different prescriptions for the implementation of the NQC correction and discussing the accuracy of each waveform mode. Focusing first on the $\ell = m = 2$ mode, we have to discuss three aspects:

(i) the impact of the precise location of the amplitude peak on the EOB temporal axis, $t^{\rm peak}_{A_{22}}$, as described by Eq. (28);
(ii) the impact of the NQC correction determined imposing also continuity between the EOB and RWZ second-time derivatives $\ddot{X}_{\rm NQC} = \{\ddot{A}_{22}^{\rm NQC}, \ddot{\omega}_{22}^{\rm NQC}\}$;
(iii) the impact due to the generic Newtonian prefactor, Eq. (20).

Note that here we are analyzing the plunge, therefore at this stage we do not consider the 2PN noncircular corrections introduced in Eq. (21). Figure 6 illustrates the analytical/numerical relative amplitude difference (dashed orange) and phase differences in radians (light blue) for all possible combinations. In the top row of the figure, the amplitude peak location is obtained according to Eq. (27), i.e., the prescription that is adopted, for simplicity, in the comparable mass case within the `TEOBResumS` model.[5] In the bottom row of the figure we consider instead its exact location according to Eq. (28). Then, moving from left to right, we add the second-time derivatives of amplitude and frequency in the NQC-corrections, the analytical generic Newtonian prefactor, and finally both effects together. In all the cases, the NQC corrections are obtained solving the system given by Eq. (25) using $t_{22}^{\rm NQC} = t^{\rm peak}_{A_{22}} + 2$.

For the $\Delta t_{\rm NQC} = 1$ case, we see that, as expected, the inclusion of both the improved NQC corrections and of the generic Newtonian prefactor brings a considerable reduction of the phase difference up to merger. Moreover, the phase difference now grows monotonically, to saturate at $\Delta\phi_{22}^{\rm EOBRWZ} \simeq 0.08$. As recently pointed out in Ref. [51], if such a behavior is reproduced for comparable-mass waveforms, generally indicates that one will end up with excellent mismatches using actual detector power spectral density. This suggests that the use of $\hat{h}_{22}^{(\rm N,0)_{\rm nc}}$ and of $\ddot{X}_{\rm NQC}$

[5]See however Ref. [52] for an early attempt to go beyond this simplifying choice.

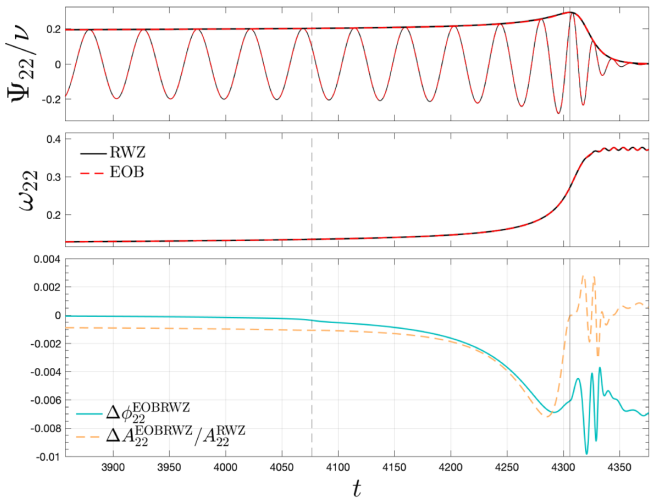

FIG. 7. Quasicircular case, $\ell = m = 2$ mode: RWZ waveform (black) compared to the complete EOB one (red, dashed). The vertical lines mark the LSO crossing and the peak of A_{22}. The bottom panel shows the relative amplitude difference (dashed orange) and the phase difference in radians (solid light blue). Non-circular corrections to the waveform up to 2PN are included.

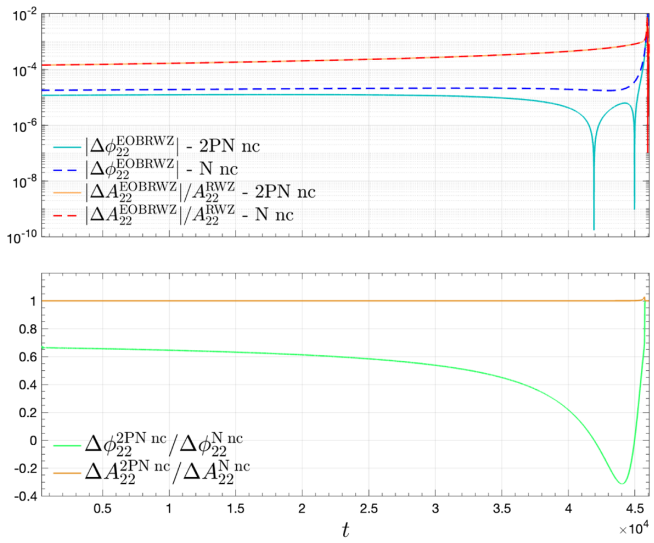

FIG. 8. EOB/RWZ phase differences (radians) and relative amplitude differences for the (2,2) mode of a quasicircular inspiral starting from $r_0 = 9$. In the upper panel we show the differences obtained with the waveform with noncircular corrections up to 2PN (solid, light blue for the phase and orange for the amplitude), and the ones obtained considering only the generic Newtonian prefactor (dashed, blue for the phase and red for the amplitude). In the bottom panel we show the ratios of these differences.

also for compable mass binaries may result in a further reduction of the current EOB/NR disagreement (∼0.2 rad) through merger and ringdown. By contrast, it is interesting to note that the amplitude difference during the ringdown is nonegligible and remains substantially unchanged whatever choice is made. When $\Delta t_{\rm NQC}^{\rm exact}$ is used we are thus not surprised to find a consistent reduction of the amplitude difference during the ringdown (though evidently it remains unchanged up to merger). By contrast, the progressive inclusion of additional physical elements (i.e. $\hat{h}_{22}^{({\rm N},0)_{\rm nc}}$ and $\ddot{X}_{\rm NQC}$) brings phase differences below 0.01 rad through the full inspiral, merger and ringdown. The complete EOB/RWZ comparison for the final quadrupolar waveform, that incorporates also 2PN noncircular corrections, is shown in Fig. 7 and complements the rightmost bottom panel of Fig. 6 also showing the EOB frequency. One appreciates that the phase difference reaches the $\sim 4 \times 10^{-4}$ rad at LSO crossing, and remains always below the 0.01 rad even at merger time. The relative amplitude difference is $\sim 1 \times 10^{-3}$ at LSO crossing to reach at most $\sim 7 \times 10^{-3}$ around merger time. Finally, we quantify the contribution of the 2PN noncircular corrections of Eq. (21) in Fig. 8, where we show the EOB/RWZ phase differences of the (2,2) mode for a quasicircular inspiral starting from $r_0 = 9$. The waveforms have been computed (i) considering the complete waveform, as discussed above and shown in Fig. 7, (ii) considering only Newtonian noncircular corrections. As can be seen, the 2PN noncircular corrections improve the phase agreement through the whole inspiral of the binary, but they are not relevant for the amplitude.

Modeling higher modes correctly using NQC corrections determined using the standard paradigm implemented in `TEOBResumS` might be tricky. The main issue is that the amplitude peak of each mode is always delayed than the (2,2) one [16], as reminded in Table II. In the discussion above we have seen that the inclusion of the generic noncircular prefactor of Eq. (19) improves the EOB/RWZ agreement for the (2,2) mode. We now proceed to evaluate the relevance of this term also for the other multipoles considering an illustrative higher mode, like the (4,4). Figure 9 shows that the waveform with only the simple quasicircular factor (dash-dotted blue line) underestimates the waveform amplitude toward merger. Starting from this, it is not possible for the waveform NQC correction to improve the waveform behavior and assure a reliable matching to the ringdown, especially for the amplitude, as shown by the NQC-corrected quasicircular waveform (dotted purple) in Fig. 9. By contrast, one sees that when the noncircular factor of Eq. (19) is used, the waveform visibly overestimates the waveform amplitude toward merger. This situation is preferable and can be easily corrected by the NQC correction, as shown by the waveform obtained computing the NQC correction at $t_{44}^{\rm NQC} = t_{A_{44}}^{\rm peak} + 2$ (yellow solid line). We also find that, in order to considerably improve the NQC corrections, the system of Eq. (25) has to be evaluated at $t_{\ell m}^{\rm NQC} < t_{A_{\ell m}}^{\rm peak}$. For all higher modes, we chose

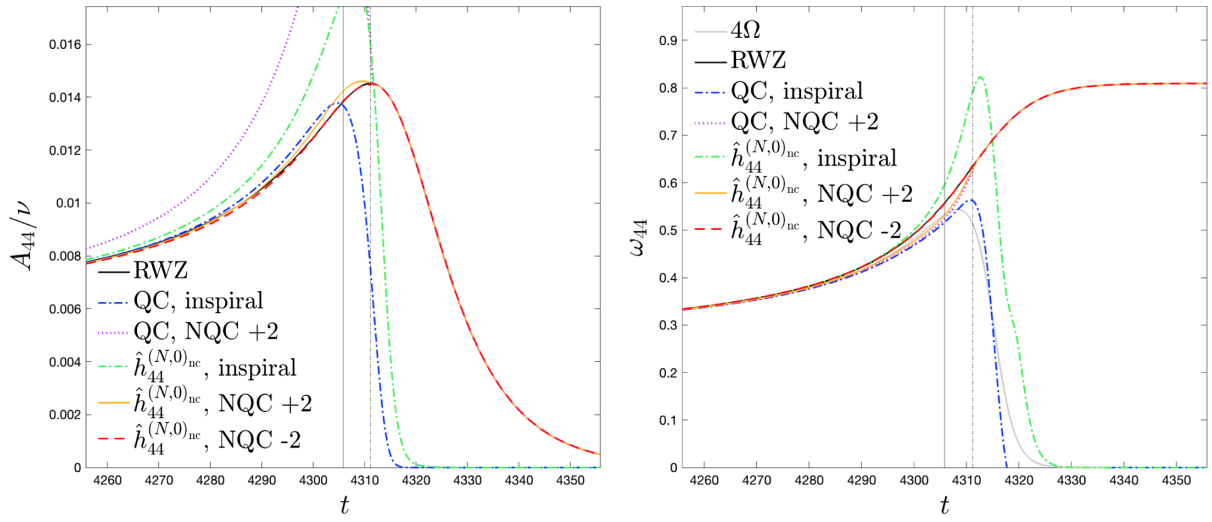

FIG. 9. Quasicircular case, mode $\ell = m = 4$: comparing various choices of analytical EOB waveform and different ways of determining the NQC corrections. Amplitude (left panel) and frequency (right panel) The best EOB/RWZ agreement is obtained by: (i) using the general, noncircular, Newtonian prefactor and (ii) when the NQC corrections are computed at $t^{\rm NQC}_{44} = t^{\rm peak}_{A_{44}} - 2$. We also show, as gray line, 4 times the orbital frequency. From left to right, the two vertical line mark $t^{\rm peak}_{A_{22}}$ and $t^{\rm peak}_{A_{44}}$.

$$t^{\rm NQC}_{\ell m} = t^{\rm peak}_{A_{\ell m}} - 2. \tag{30}$$

Therefore, to compute the right-hand side of Eq. (25), we need to fit $\{A^{\rm NQC}_{\ell m}, \dot{A}^{\rm NQC}_{\ell m}, \ddot{A}^{\rm NQC}_{\ell m}, \omega^{\rm NQC}_{\ell m}, \dot{\omega}^{\rm NQC}_{\ell m}, \ddot{\omega}^{\rm NQC}_{\ell m}\}$ from RWZ data. The global fits are discussed in Appendix C and reported in Tables VII and VIII. The (4,4) multipole with the generic Newtonian prefactor and the NQC evaluated according to Eq. (30) is shown with a red dashed line in Fig. 9. As can be seen, both the amplitude and the frequency improves near the matching time with respect to the waveforms with NQC computed at $t^{\rm NQC}_{44} = t^{\rm peak}_{A_{44}} + 2$.

For $\ell = m$ modes, we use the same prescriptions of the (2,2) mode, except for the fact that the NQC corrections are computed before the peak amplitude, according to Eq. (30). The results for the (3,3), (4,4), and (5,5) modes are shown in the top row of Fig. 10, where we use the color black for the numerical waveform and frequency and red dashed lines for the complete EOB waveform. The absolute value of phase difference, is always below 0.07, 0.035 and 0.05 radians for the (3,3), (4,4), and (5,5) modes, respectively. The relative amplitude difference, instead, is around at most of the 1% before the matching point for all the three cases. However, the amplitude difference in the late ringdown is around the 10^{-3} for the (3,3) and (4,4) modes and even smaller (8×10^{-4}) for the (5,5) mode.

The $m < \ell$ modes are shown in the middle and bottom rows of Fig. 10. In this case we do not consider the second-time derivative of the frequency in the NQC corrections. As for the higher modes with $\ell = m$, the NQC are computed at $t^{\rm NQC}_{\ell m} = t^{\rm peak}_{A_{\ell m}} - 2$. However, for the $m < \ell$ we also apply a downsampling and spline procedure in the interval $t \in [t^{\rm NQC}_{\ell m}, t^{\rm peak}_{A_{\ell m}}]$ to improve the continuity of the waveform. Indeed, since the NQC corrections are determined at $t^{\rm NQC}_{\ell m}$, the waveform could be discontinuous at $t^{\rm peak}_{A_{\ell m}}$, where the NQC-corrected plunge waveform is matched to the ringdown. The downsampling and subsequent spline-patching solves this issue. While these higher modes are less accurate than the $\ell = m$ ones, the phase agreement is still good and generally below the 0.2 rad, with the exception of the (4,2) and (4,1) modes that are more de-phased. The degradation of the accuracy is strictly linked to the higher delay of the matching point (i.e. $t^{\rm peak}_{A_{\ell m}}$); see Table II. However, these modes are not relevant as the others in the complete strain, that can be computed using Eq. (5). In the first panel of Fig. 13 we show the strain for the observational direction $(\Theta, \Phi) = (\pi/4, 0)$ computed considering all the modes shown so far, both in the numerical and analytical strain. During the inspiral, the relative amplitude difference reaches at most the 2×10^{-3}, while the absolute value of the phase difference never exceeds the 2×10^{-3} radians. The differences oscillate more in the ringdown; the amplitude difference reaches at most the 8% in the early ringdown, while the phase difference reaches at most 0.06 radians. Note however that, on average, during the ringdown both the amplitude and the phase difference are much smaller.

B. The eccentric case

Let us move now to discussing the eccentric case. The same procedures considered optimal in the quasicircular case are retained also in the presence of eccentricity so to provide comparisons with the eccentric configurations

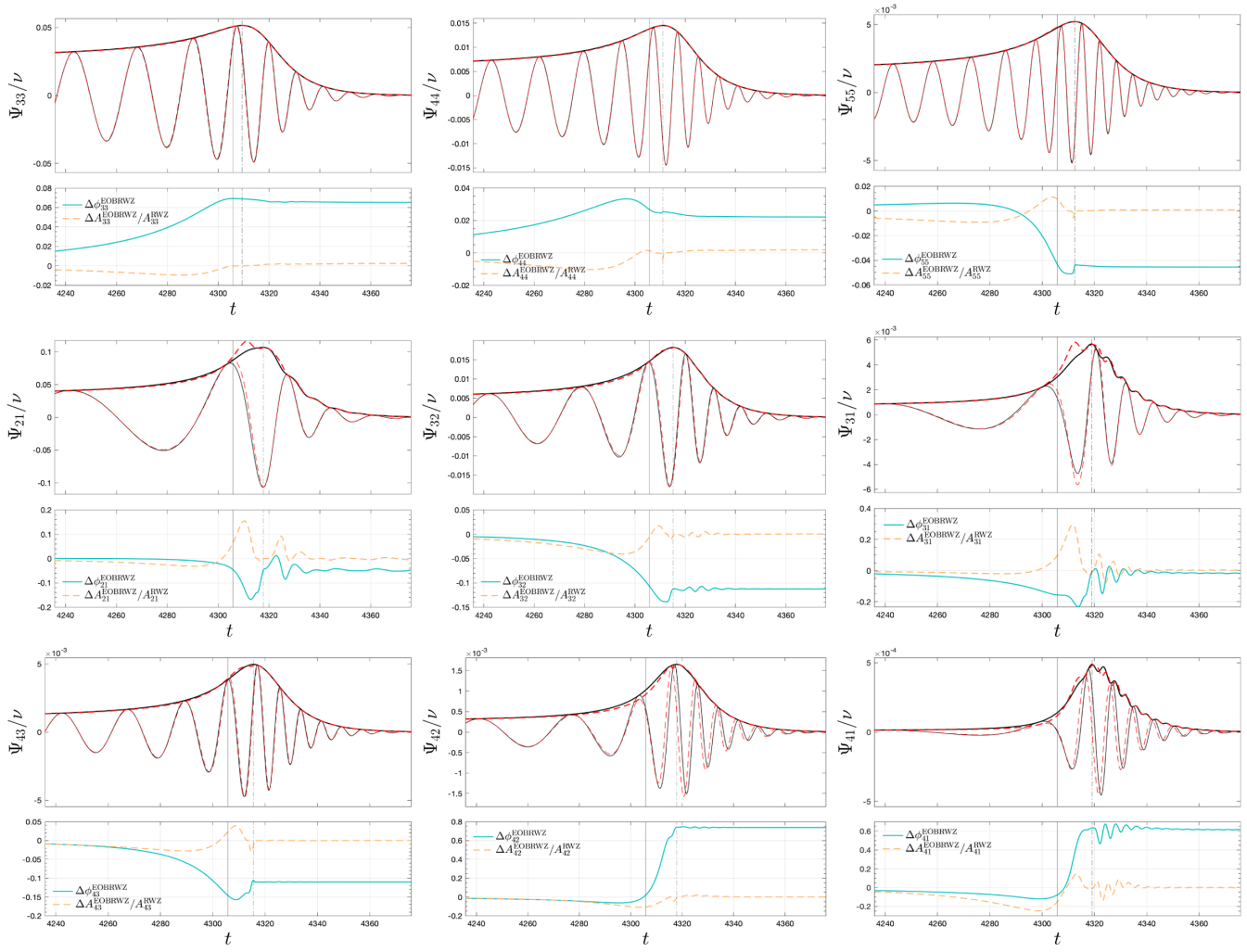

FIG. 10. Quasicircular configuration, higher modes, EOB/RWZ comparisons. The vertical solid black lines mark $t^{\rm peak}_{A_{22}}$, while the dash-dotted ones mark $t^{\rm peak}_{A_{\ell m}}$. Bottom panels: relative amplitude difference (orange, dashed) and phase difference (light blue). For each mode, the NQC corrections are determined according to the best prescription selected in Fig. 9.

listed in Table I. As an explicit example that efficiently summarizes the performance of the model all over the parameter space, Fig. 11 shows the EOB/RWZ performance for configuration #20 of Table I, that corresponds to initial eccentricity $e_0 = 0.95$. Note that this configuration is not used in the global fits, as discussed in Sec. II E. The figure includes modes (2,2), (2,1), and (3,3). The performance of the model all over the RWZ-covered points of the parameter space is assessed, for the same waveform multipoles, in Fig. 12, that only reports relative amplitude differences (top row plots) and phase differences (bottom row plots). Note that three specific configurations are highlighted in color, so to point out that the performance of the model degrades (slightly) as eccentricity is increased. The simplest route to have a handle on the accuracy of all multipoles is simply to compare the strain for EOB and RWZ. This is done in Fig. 13 for the quasicircular case, for $e_0 = 0.55$ and for $e_0 = 0.95$. It is interesting to note that, despite the EOB performance during the (eccentric) inspiral degrades with eccentricity, as expected, due to the lack of high-order corrections (see Refs. [48,49]), the behavior during merger and ringdown is practically comparable among the three cases.

C. Improved description of ringdown for $m \neq \ell$ modes

So far, we have seen that the EOB waveform model gives more than satisfactory results also for the higher modes. However, if one carefully inspects the $m = 1$ EOB modes in the quasicircular case (see Fig. 10), one sees the ubiquitous presence of a bump before the actual amplitude peak. Interestingly, this feature occurs in all modes and it is related to the NQC amplitude correction. In general, this is also true for other modes with $m \neq \ell$, though the effect is less visible. To overcome this difficulty, we decided to explore a different way to model the ringdown for higher

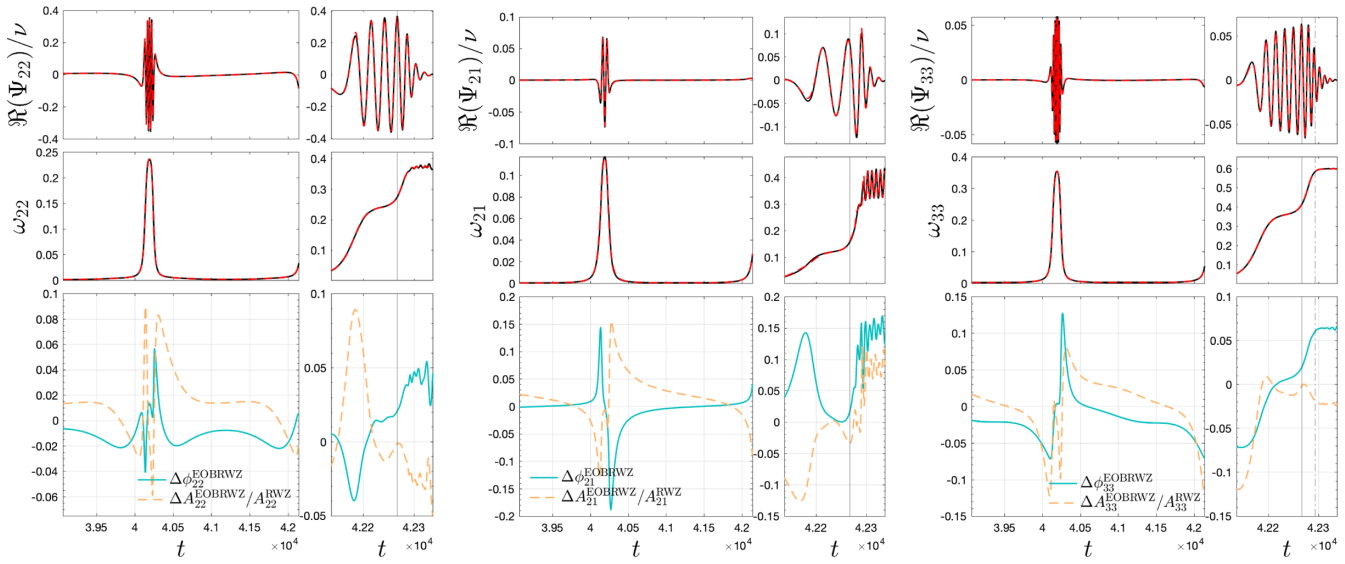

FIG. 11. Analytical/numerical comparisons for the (2,2), (2,1), and (3,3) multipoles for the configuration with initial eccentricity $e_0 = 0.95$. We show the real part and the frequency of the RWZ waveform (black) and the complete EOB waveform (red, dashed). In the bottom panels we show the relative amplitude difference (orange dashed) and the phase difference in radians (light blue). The vertical solid lines mark the peak of A_{22}, while the dash-dotted ones mark $t^{\rm peak}_{A_{\ell m}}$.

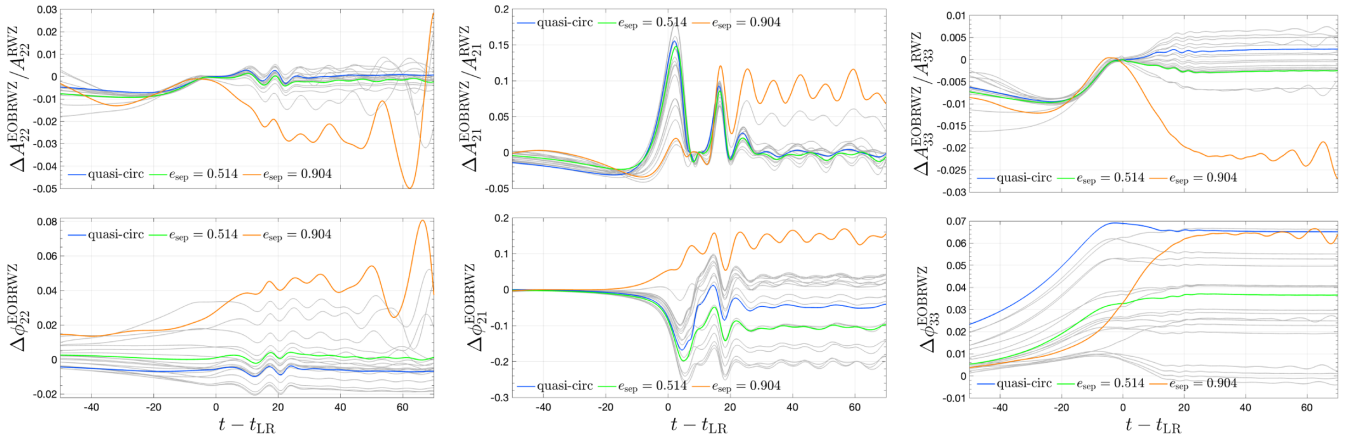

FIG. 12. Analytical/numerical relative difference for the amplitude (upper panels) and phase difference (bottom panels) for the plunge-ringdown of all the configurations considered in this work. Modes (2,2), (2,1), and (3,3). We highlight the quasicircular configuration (blue) and the ones with $e_0 = \{0.55, 0.95\}$ (green and orange, respectively).

modes. The procedure is substantially the same used in the EOB models of the SEOBNR-family, in particular SEOBNRv4PHM [53,54] and SEOBNRv5PHM [55,56], although the fitting template is different from the one used there. This approach is crucial to obtain very reliable waveforms when $t^{\rm peak}_{A_{\ell m}}$ is far from $t^{\rm peak}_{A_{22}}$, i.e., situations where the NQC corrections cannot guarantee a reliable match of the plunge waveform to the merger ringdown one modeled after $t^{\rm peak}_{A_{\ell m}}$. The main idea is to have the RWZ-informed part of the waveform starting directly from $t^{\rm peak}_{A_{22}}$ (and not from $t^{\rm peak}_{A_{\ell m}}$) for all modes with $\ell \neq m$. To do so, we consider the QNM-rescaled waveform similar to the one of Eq. (9), but where the time is shifted using $t^{\rm peak}_{A_{22}}$ for each (ℓ, m) mode. It thus reads

$$\bar{h}_{\ell m}(\bar{\tau}) = e^{\sigma^{+}_{\ell m 1}\bar{\tau} + i\phi^{0}_{\ell m}} h^{\rm rng}_{\ell m}(\bar{\tau}), \tag{31}$$

where $\bar{\tau} \equiv t - t^{\rm peak}_{A_{22}}$ and $\phi^0_{\ell m}$ is the phase of the (ℓ, m) multipole at $t^{\rm peak}_{A_{22}}$. This rescaled waveform is then written as $\bar{h}^{\rm mod}_{\ell m}(\bar{\tau}) = A_{\bar{h}} e^{i\phi_{\bar{h}}}$, where the templates for $A_{\bar{h}}$ and $\phi_{\bar{h}}$ are given in Eqs. (10) and (11). We impose continuity conditions constraining c^A_1, c^A_2, c^A_4, and c^ϕ_1:

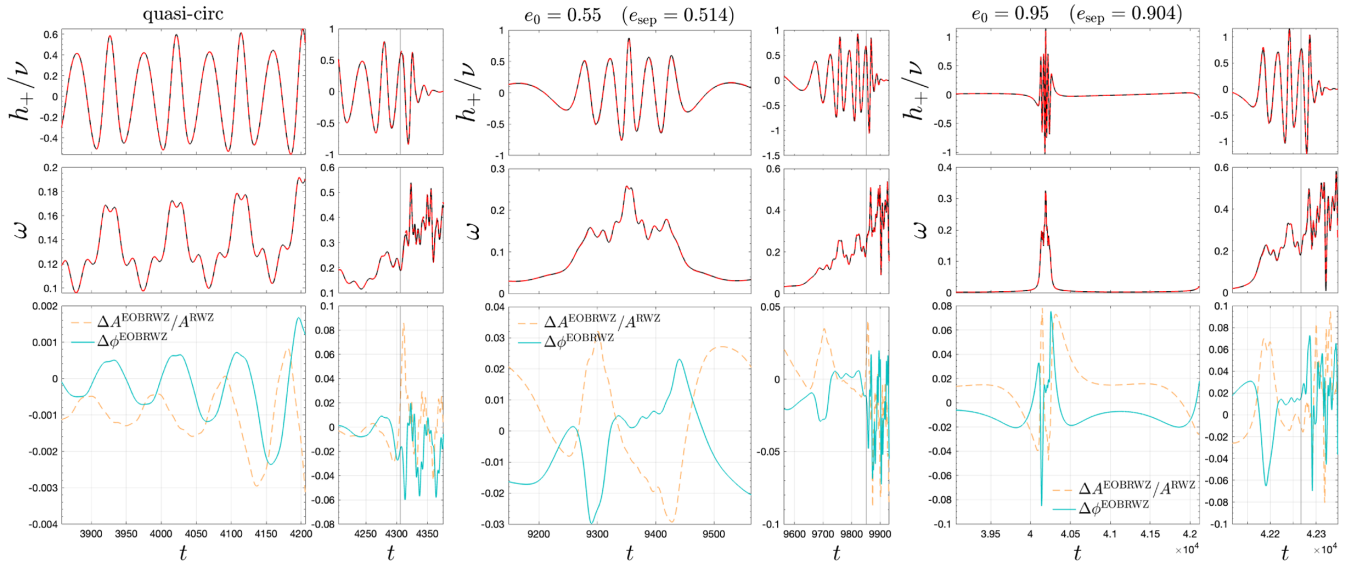

FIG. 13. EOB (red dashed) versus RWZ (black, solid) strain comparison for $e_0 = \{0, 0.55, 0.95\}$. The direction is $(\Theta, \Phi) = (\pi/4, 0)$ and all modes with $m > 0$ are summed up to $\ell = 4$, plus the (5,5) one. Bottom panels: relative amplitude difference and phase difference (in radians). The vertical lines mark the peak of the quadrupolar amplitude.

$$c_1^A = e^{-c_3^A}(e^{2c_3^A} - 1)c_5^A \left(A_{t^{\rm peak}_{A_{22}}}\right)^{c_5^A} \left(\alpha_1 A_{t^{\rm peak}_{A_{22}}} + \dot{A}_{t^{\rm peak}_{A_{22}}}\right)^2 \times \left[\alpha_1^2 \left(A_{t^{\rm peak}_{A_{22}}}\right)^2 c_5^A + A_{t^{\rm peak}_{A_{22}}} \left(2\alpha_1 c_5^A \dot{A}_{t^{\rm peak}_{A_{22}}} + \ddot{A}_{t^{\rm peak}_{A_{22}}}\right) + (c_5^A - 1)\left(\dot{A}_{t^{\rm peak}_{A_{22}}}\right)^2\right]^{-1}, \tag{32}$$

$$c_2^A = \frac{c_5^A}{c_1^A} e^{-c_3^A}(e^{c_3^A} + 1)^2 \left(A_{t^{\rm peak}_{A_{22}}}\right)^{c_5^A - 1} \left[\alpha_1 A_{t^{\rm peak}_{A_{22}}} + \dot{A}_{t^{\rm peak}_{A_{22}}}\right], \tag{33}$$

$$c_4^A = (A_{t^{\rm peak}_{A_{22}}})^{c_5^A} - \frac{c_1^A}{e^{c_3^A} + 1}, \tag{34}$$

$$c_1^\phi = \frac{1 + c_3^\phi + c_4^\phi}{c_2^\phi (c_3^\phi + 2c_4^\phi)} \left(\omega_1 - \omega_{t^{\rm peak}_{A_{22}}}\right), \tag{35}$$

where $A_{t^{\rm peak}_{A_{22}}}$, $\dot{A}_{t^{\rm peak}_{A_{22}}}$, $\ddot{A}_{t^{\rm peak}_{A_{22}}}$, and $\omega_{t^{\rm peak}_{A_{22}}}$ are, respectively, the amplitude of $h_{\ell m}$, its first and second time derivative and the frequency evaluated at $t^{\rm peak}_{A_{22}}$; $\alpha_1 + i\omega_1$ is the ℓ-fundamental QNM frequency. The coefficients $\{c_3^A, c_5^A, c_2^\phi, c_3^\phi, c_4^\phi\}$ are determined performing the primary fits of $A_{\bar{h}}$ and $\phi_{\bar{h}}$ starting from $t^{\rm peak}_{A_{22}}$. Finally, this fitted waveform is used to determine the NQC corrections at $t^{\rm peak}_{A_{22}}$ and then is matched to the inspiral wave, always at $t^{\rm peak}_{A_{22}}$. Concerning the structure of the NQC correction to amplitude and phase, there is an additional subtlety. We realized that the standard NQC basis we used so far is not efficient when the NQC corrections are determined at $t^{\rm peak}_{A_{22}}$ for $m \neq \ell$, and it is thus better to resort to the NQC basis used by `SEOBNRv5PHM` that reads

$$n_1 = \frac{p_{r_*}^2}{(r\Omega)^2}, \tag{36}$$

$$n_2 = \frac{n_1}{r}, \tag{37}$$

$$n_3 = n_1 r^{-3/2}, \tag{38}$$

$$n_4 = \frac{p_{r_*}}{r\Omega}, \tag{39}$$

$$n_5 = n_4 p_{r_*}^2. \tag{40}$$

The real part, amplitude and frequency of the final result for the (2,1) and (4,1) modes are shown in Fig. 14. It is remarkable how the different NQC approach can visibly improve the EOB/RWZ agreement. The only visible remaining differences between the two curves (mostly around the waveform peak) are related to the fact that the mode mixing only includes the fundamental mode and not the overtones.

Although the improvement discussed in the nonspinning case may be considered relatively marginal, it becomes absolutely essential when the central black hole is spinning and the spin is large and antialigned with the orbital angular momentum. In this case, the orbital frequency has a zero and thus the NQC basis becomes meaningless. This is clarified in Fig. 15, that refers to the (2,1) mode for a particle inspiralling and plunging on a Kerr black hole with dimensionless spin $\hat{a} = -0.9$, where the numerical (black) waveform has been obtained with the time-domain code [57]. As the orbital frequency (gray online) passes through zero, the NQC corrected waveform determined using the standard approach oscillates unphysically. By contrast, the NQC correction

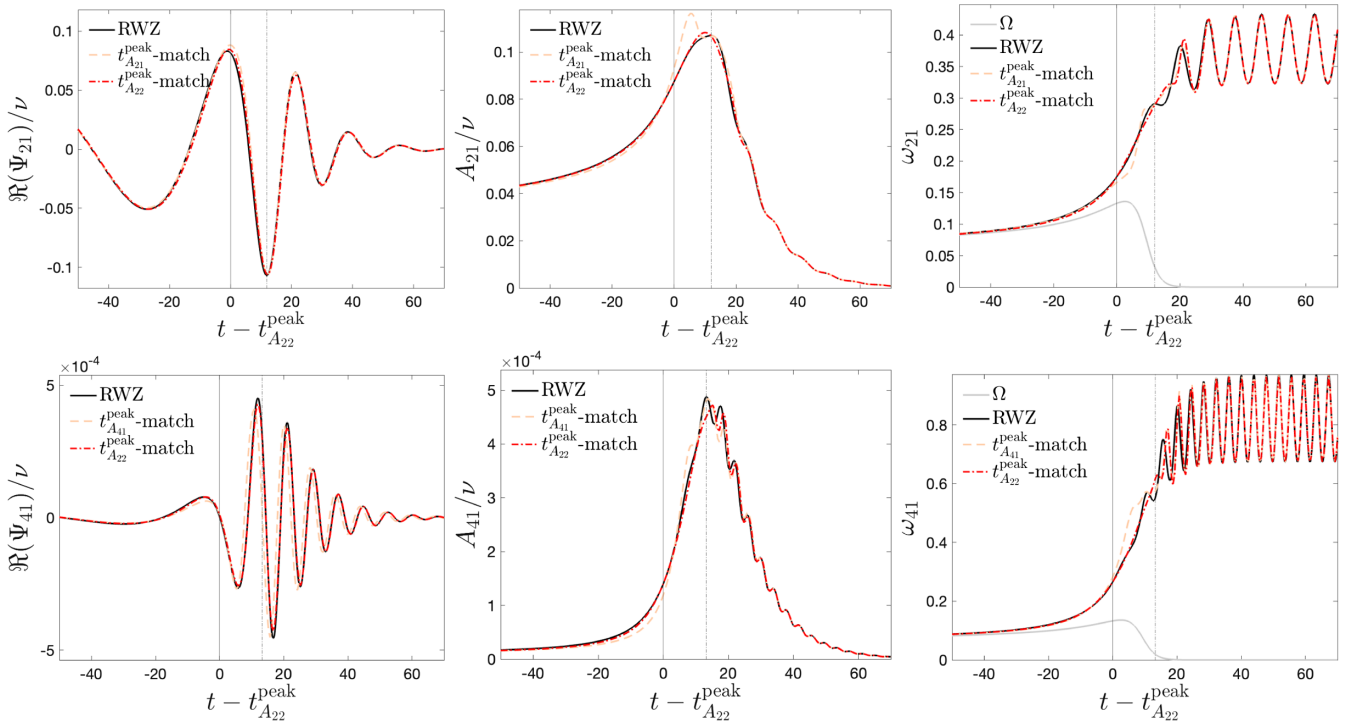

FIG. 14. Nonspinning case. New ringdown (red dashed) contrasted with the standard one discussed above (orange, dashed) for the (2,1) and (4,1) modes. The RWZ ringdown waveform is fitted from $t^{\rm peak}_{A_{22}}$ (solid vertical lines) rather than from $t^{\rm peak}_{A_{\ell m}}$ (dash-dotted vertical lines). This ensures a more accurate waveform description around $t^{\rm peak}_{A_{\ell m}}$.

determined at $t^{\rm peak}_{A_{22}}$, using the basis of Eqs. (36)–(40) allows one to smoothly and reliably connect the inspiral waveform to the ringdown one. In this preliminary study, we are evidently not considering the mode mixing during the Kerr ringdown [58], so the EOB frequency and amplitude do not present any modulation.

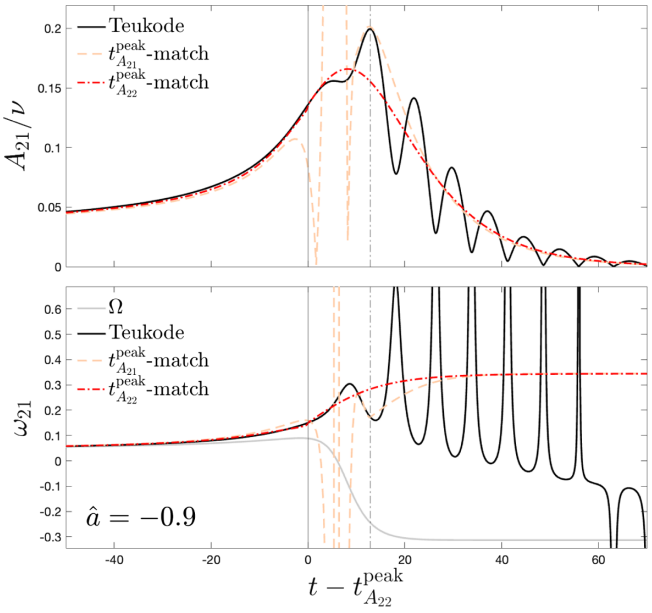

FIG. 15. Spinning case with Kerr parameter $\hat{a} = -0.9$. The NQC and ringdown determined from $t^{\rm peak}_{A_{22}}$ instead of $t^{\rm peak}_{A_{\ell m}}$ allow for an excellent EOB/Teukode agreement. Note that the mode mixing in this case is not implemented in the EOB waveform.

V. PHENOMENOLOGY OF QUASINORMAL-MODES EXCITATION

In the previous section we have provided an accurate and complete EOB waveform where the ringdown model was based on a phenomenological description. In doing so, we assumed that the fundamental QNM was excited, but we did not attempt any qualitative (nor quantitative) investigation to understand the origin of this excitation. In this section we attempt to do this, still in a somehow phenomenological and heuristic way. Our main aim is to correlate the QNMs excitation with the behavior of the source of the RWZ equations that is driven by the dynamics. The material presented here is inspired by and extends the (qualitative) discussion of Sec. III B of Ref. [13] (see also Fig. 4 therein).

A. The RWZ source term during ringdown

We start by analyzing the source terms of the RWZ equations, Eq. (6). Their functional form is [15]

$$S^{(\rm o/e)}_{\ell m} = \bar{G}^{(\rm o/e)}_{\ell m}(\tilde{r},t)\delta(\tilde{r}_* - r_*(t)) + \bar{F}^{(\rm o/e)}_{\ell m}(\tilde{r},t)\partial_{\tilde{r}_*}\delta(\tilde{r}_* - r_*(t)), \tag{41}$$

where the tilde denotes the field tortoise coordinate, while $r_*(t)$ is the tortoise coordinate of the particle. In order to understand the relevance of the source terms during the ringdown, we evaluate it on the particle dynamics. More precisely, we neglect the term proportional to $\partial_{\tilde{r}_*}\delta(\tilde{r}_* - r_*(t))$ in Eq. (41) and just evaluate $\bar{G}^{(\mathrm{o/e})}_{\ell m}$. This yields the expressions

$$F^{(\mathrm{e})}_{\ell m}(t) \equiv \frac{16\pi\mu Y^*_{\ell m}}{r\hat{H}\lambda[r(\lambda-2)+6]}\left\{2imAp_{r_*}p_\varphi - A\left[3\left(1+\frac{4\hat{H}^2 r}{r(\lambda-2)+6}\right)-\frac{r\lambda}{2} + \frac{p_\varphi^2}{r^2(\lambda-2)}(r(\lambda-2)(m^2-\lambda-1) + 2(3m^2-\lambda-5)) + \frac{2}{r^2}(p_\varphi^2+r^2)\right]\right\}, \tag{42a}$$

$$F^{(\mathrm{o})}_{\ell m}(t) \equiv \frac{16\pi\mu\partial_\Theta Y^*_{\ell m}}{r\lambda(\lambda-2)}\left[\frac{d}{dt}\left(\frac{p_{r_*}p_\varphi}{\hat{H}}\right) - 2\frac{p_\varphi A}{r} - im\frac{Ap_{r_*}p_\varphi^2}{r^2\hat{H}^2}\right], \tag{42b}$$

where $\lambda \equiv \ell(\ell+1)$. After having set $\Theta = \pi/2$, we show $|F^{(\mathrm{o/e})}_{\ell m}(t)|$ for the (2,2) mode in Fig. 16. Interestingly, $|F^{(\mathrm{e})}_{22}(t)|$ reaches its maximum after the peak of A_{22} and remains quite relevant also later on. For example, at $t = t^{\mathrm{peak}}_{A_{22}} + 10$ we have $\hat{F}^{(\mathrm{e})}_{22} \equiv |F^{(\mathrm{e})}_{22}|/\max(|F^{(\mathrm{e})}_{22}|) \simeq 0.38$, and $\hat{F}^{(\mathrm{e})}_{22} < 10^{-2}$ only from $t = t^{\mathrm{peak}}_{A_{22}} + 18.2$. For the odd modes we have that the maximum of the source is delayed with respect to the even ones. Since the source term is quite relevant during the ringdown, we do not expect *a priori* that a pure QNMs description (i.e., part of the solution of the homogeneous RWZ equations) can be used for the whole postpeak waveform. However, from a sufficient late time $t > t^{\mathrm{peak}}_{A_{\ell m}}$, the (ℓ, m)-mode can be fully described in terms of QNMs using the ansatz of Eq. (8) since the source term becomes negligible.

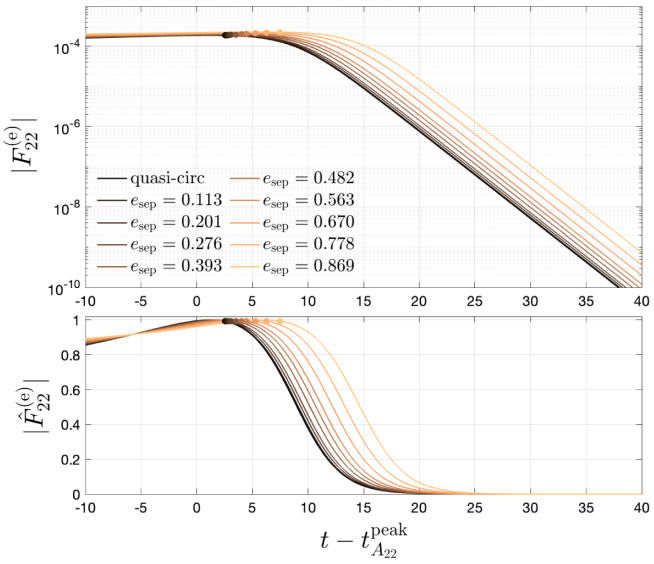

FIG. 16. Upper panel: Zerilli source term evaluated along dynamics with different eccentricities for the (2,2) mode. Logarithmic vertical scale. Bottom panel: plot of $\hat{F}^{(\mathrm{e})}_{22} = |F^{(\mathrm{e})}_{22}|/\max(|F^{(\mathrm{e})}_{22}|)$. The retarded time is shifted using the peak time of the quadrupolar amplitude, $t^{\mathrm{peak}}_{A_{22}}$. In both panels, the dots mark the light-ring crossing, t_{LR}.

B. Iterative time-domain fit of the postpeak frequency

We thus proceed to fit the late ringdown waveform assuming that is given by a linear superposition of QNMs with constant coefficients, see Eq. (8), using $\tau = t - t^{\mathrm{peak}}_{A_{\ell m}}$. The total QNM frequency of each multipole is obtained as

$$\omega^{(\mathrm{o/e})}_{\ell m} = -\Im\left(\frac{\dot{\Psi}^{(\mathrm{o/e})}_{\ell m}}{\Psi^{(\mathrm{o/e})}_{\ell m}}\right) = -\Im\left[\frac{\sum_{n=1}^{\infty}\bar{b}_{\ell mn}\frac{\sigma^+_{\ell n}}{\sigma^+_{\ell 1}}e^{(\sigma^+_{\ell 1}-\sigma^+_{\ell n})\tau}(1+\hat{a}_{\ell mn}\frac{\sigma^-_{\ell n}}{\sigma^+_{\ell n}}e^{2i\omega_{\ell n}\tau})}{\sum_{n=1}^{\infty}\bar{b}_{\ell mn}e^{(\sigma^+_{\ell 1}-\sigma^+_{\ell n})\tau}(1+\hat{a}_{\ell mn}e^{2i\omega_{\ell n}\tau})}\right], \tag{43}$$

where $\hat{a}_{\ell mn} = C^-_{\ell mn}/C^+_{\ell mn}$ and $\bar{b}_{\ell mn} = C^+_{\ell mn}/C^+_{\ell m1}$. Since these are complex quantities, we define $\hat{a}_{\ell mn} \equiv \hat{A}_{\ell mn}e^{i\hat{\theta}_{\ell mn}}$ and $\bar{b}_{\ell mn} \equiv \bar{B}_{\ell mn}e^{i\bar{\phi}_{\ell mn}}$. Recalling the hierarchy of the inverse damping times $\alpha_{\ell n}$, the contributions in the frequency of the $n \geq 1$ overtones are exponentially damped with exponents $\alpha^+_{\ell 1} - \alpha^+_{\ell n}$. However, the contribution of the isolated fundamental frequencies is never damped and reads

$$\omega^{(\mathrm{o/e})}_{\ell m1} = \frac{(1-\hat{A}^2_{\ell m1})\omega_{\ell 1}}{1+\hat{A}^2_{\ell m1}+2\hat{A}^2_{\ell m1}\cos(2\omega_{\ell 1}\tau+\hat{\theta}_{\ell m1})}. \tag{44}$$

The coefficients $\hat{A}_{\ell m1}$ and $\theta_{\ell m1}$ were already extracted from the late ringdown frequency in previous works [16,58]. Here we extend this procedure to earlier times using Eq. (43). Since the overtones have higher damping coefficients, we proceed to iteratively fit the late ringdown frequency on different time intervals considering only the relevant QNMs. To establish where a certain n mode becomes negligible, we set a small threshold, typically $\epsilon = 10^{-5}$, and we say that the nth-mode can be neglected if the condition $e^{(\alpha^+_{\ell 1}-\alpha^+_{\ell n})\tau} < \epsilon$ is satisfied. Applying this method to the (2,2) mode we can find $\{\hat{A}_{22n}, \hat{\theta}_{22n}, \bar{B}_{22n}, \bar{\phi}_{22n}\}$ up to $n = 4$. The results are shown in Fig. 17. It is interesting to note that for the (2,2) mode

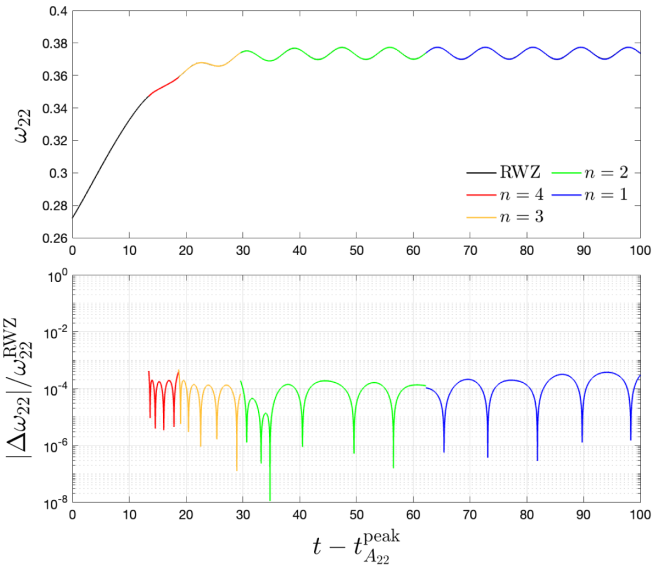

FIG. 17. Iterative QNM-fit of the frequency considering the first 4 QNMs. In the upper panel we show the RWZ frequency (black) and the results obtained with the fits. Each color represents an iteration (and thus a QNM) of the fit. In the bottom panel we show the relative difference between the fit and the corresponding n fit. See Sec. V B for more detail on the fitting procedure.

we are not able to go beyond $n=4$ and thus at earlier times. This can be justified by the discussion on the source term above. Indeed, with $n=4$ and $\epsilon=10^{-5}$ we are able to fit from $t=13.43$, but at that time we still have $|F^{(e)}_{22}|/\max(|F^{(e)}_{22}|)\simeq 0.097$ and thus the source term is not completely negligible. Also for this reason, the values of $\hat{a}_{22n}$ and $\bar{b}_{22n}$ found for the overtones are not robust and are in disagreement with the results found using the different fitting procedures (see Appendix B). The procedure can be applied also to the higher modes, where the number of overtones that we are able to fit depends on the specific multipole considered. Generally, we have that for the modes with higher $\Delta t_{\ell m}$ (i.e., the for the ones that are more delayed), we are able to fit more overtones, consistently with the fact that at later times the source terms become negligible. For example, for the (4,1) multipole we can fit up to $n=7$ overtones (and thus from $t\simeq t^{\rm peak}_{41}+5.94$) keeping the relative error of the frequency fit around 10^{-4}.

From a practical point of view, we are particularly interested in the values related to the fundamental frequencies, $\hat{a}_{\ell m1}$, since we can use them to improve the phenomenological ringdown description as discussed in Sec. III, see in particular Eq. (16). The values found in this work are in agreement with previous work [16] and their modulus is reported in Table III. Note that the order of magnitude of $\hat{A}_{\ell m1}$ is strictly linked to the number m and does not strongly depended on the eccentricity (see, e.g., the right panel of Fig. 4). Therefore, we need to perform the global fits only on the phases $\theta_{\ell m1}$, that we report in Table IV for all the multipoles considered in this work. The relevance of these fits can be particularly appreciated looking at the analytical/numerical comparisons of the late-ringdown waveform frequencies shown in Figs. 7, 11, and 14.

Finally, we mention that since the iterative fit of the frequency did not provide satisfactory results for the whole quadrupolar postpeak waveform, we also attempted the same fit *without* the iterative procedure, focusing only on the (2,2) multipole. However, also this procedure did not lead to robust results for the whole postpeak waveform, as detailed in Appendix B.

TABLE III. Coefficients $\hat{A}_{\ell m1}=|\hat{a}_{\ell m1}|$ describing the beating between positive and negative frequencies fundamental QNMs for all multipoles up to $\ell=6$. See Table IV for the eccentric fits of the $\hat{a}_{\ell m1}$ phase.

$\hat{A}_{\ell m1}$	$m=1$ $[\times10^{-2}]$	$m=2$ $[\times10^{-3}]$	$m=3$ $[\times10^{-4}]$	$m=4$ $[\times10^{-5}]$	$m=5$ $[\times10^{-6}]$	$m=6$ $[\times10^{-7}]$
$\ell=2$	7.30	4.89				
$\ell=3$	9.34	7.96	5.53			
$\ell=4$	9.14	9.11	8.90	6.28		
$\ell=5$	9.41	8.97	9.27	9.96	7.02	
$\ell=6$	9.46	9.12	9.11	9.67	11.15	8.33

TABLE IV. Global fits for the beating coefficients $\hat{a}_{\ell m1}=\hat{A}_{\ell m1}e^{i\theta_{\ell m1}}$. The template used for the phase is $\theta_{\ell m1}=(C^{\theta}_{\rm QC}+C^{\theta}_1\hat{b}_{\Omega_{\rm pk}}+C^{\theta}_2\hat{b}^2_{\Omega_{\rm pk}})/(1+D^{\theta}_1\hat{b}_{\Omega_{\rm pk}})$, while the modulus does not depend on the nature of the perturbation.

(ℓ,m)	$\hat{A}_{\ell m1}$	$C^{\theta}_{\rm QC}$	C^{θ}_1	C^{θ}_2	D^{θ}_1
(2,2)	4.89×10^{-3}	5.369	−9.444	−37.992	…
(2,1)	7.30×10^{-2}	2.893	−6.074	−15.134	−2.105
(3,3)	5.53×10^{-4}	2.636	−11.635	−9.555	…
(3,2)	7.96×10^{-3}	4.649	−3.890	−0.1176	…
(3,1)	9.34×10^{-2}	3.810	0.3296	−0.03943	…
(4,4)	6.28×10^{-5}	6.503	−13.096	−8.815	…
(4,3)	8.90×10^{-4}	2.453	−6.041	−1.309	…
(4,2)	9.11×10^{-3}	1.186	−2.772	−0.4334	…
(4,1)	9.14×10^{-2}	3.714	0.3582	0.1166	…
(5,5)	7.02×10^{-6}	4.509	−15.344	−4.330	…

C. EOB ringdown as superposition of QNMs

In the previous sections we have accumulated results which indicate that the ringdown description as linear superposition of QNMs with constants coefficients, Eq. (8) cannot be consistently used for the whole postpeak waveform. However, in seminal EOB works [13,59] the ringdown was modeled precisely in this way, although it was matched with the inspiral part of the waveform on an extended interval centered around the peak of the orbital

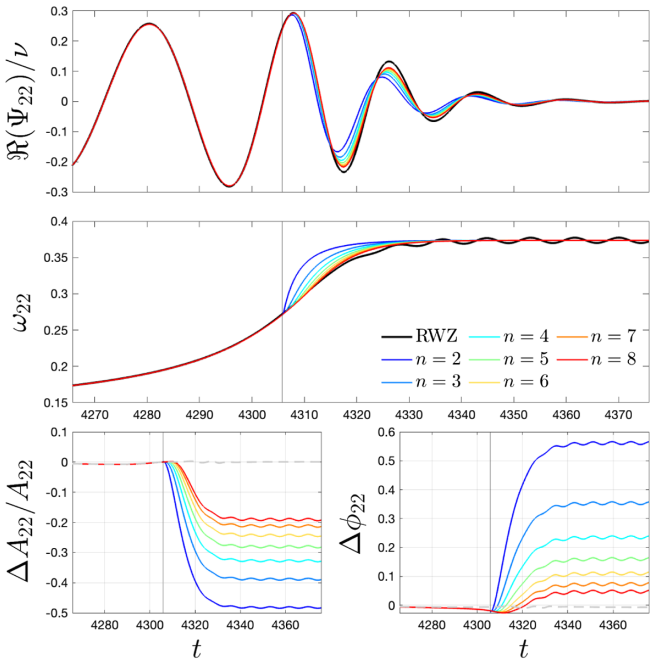

FIG. 18. EOB waveform where the ringdown has been modeled with the matching comb procedure. In the bigger panels above we show the real part of the waveform and its frequency, black for the RWZ results and online colors for the analytical results. In the two small bottom panels we show the relative amplitude difference and the phase difference with the same color scheme of the upper panels. We also show the relative amplitude difference and the phase difference obtained with the waveform model discussed in Sec. IV (dashed gray).

frequency. We will now revisit this procedure, often referred to as "matching comb" [13]. The basic idea of this procedure is that the match is performed on a set of points rather than at only one point. To determine the complex coefficients $C^{\pm}_{\ell mn}$, we solve the linear system $h_{\ell m}(t_i) = \sum C^{\pm}_{\ell mn} e^{-\sigma^{\pm}_{\ell n} t_i}$, where t_i are the points of the time array used for the match, and $h_{\ell m} = h^{\rm inspl}\hat{h}^{\rm NQC}_{\ell m}$ is the NQC-corrected inspiral waveform. If we consider N QNMs (distinguished between positive and negative frequency), we then need N points. Note that this ringdown model does not require any tuned numerical parameters, it only needs the QNMs frequencies since the coefficients of the ringdown are determined using the analytical waveform. Similarly to what discussed in Sec. IV for the (2,2) waveform multipole, we use $\{A^{\rm NQC}_{22}, \dot{A}^{\rm NQC}_{22}, \ddot{A}^{\rm NQC}_{22}, \omega^{\rm NQC}_{22}, \dot{\omega}^{\rm NQC}_{22}, \ddot{\omega}^{\rm NQC}_{22}\}$, but here we directly extract them from the Zerilli waveform at $t^{\rm NQC}_{22} = t^{\rm peak}_{A_{22}} + 2$. We chose as matching points the adjacent points to $t^{\rm peak}_{A_{22}}$ in the time grid used to solve numerically the Hamilton's equations (1). The results of this procedure are shown from $n = 2$ up to $n = 8$ in Fig. 18. The configuration that reproduces the numerical waveform with the highest accuracy is the one with $n = 8$ positive-frequency modes. For this configuration, in the late ringdown we have a 18% relative amplitude difference and a phase difference that oscillates around the 0.04 radians. We also show the relative amplitude difference and the phase difference obtained with the state-of-the-art waveform discussed in Sec. IV (dashed gray). While the waveform obtained with the latter model is clearly more accurate (see also Fig. 7 for comparison), the results obtained in this section are still qualitatively good for the amplitude and quite accurate for the phase.

D. Tail contribution

Having considered only the first part of the waveform, we have so far neglected the power-tail effects in the waveform [60,61]. However, since the QNMs are exponentially damped, there is a time where the tail effects become dominant. As can be seen from the frequency of the Zerilli (2,2) quasicircular waveform shown in black in the left panel of Fig. 19, the effect of the tail starts to be visible at $t \sim t^{\rm peak}_{A_{22}} + 170$, and becomes dominant shortly afterward. In order to reproduce the numerical waveform, we have to include a term of the form $C^{\rm tail}_{22}\tau^{-2-\ell}$, where the complex coefficient $C^{\rm tail}_{22}$ is determined with a fit

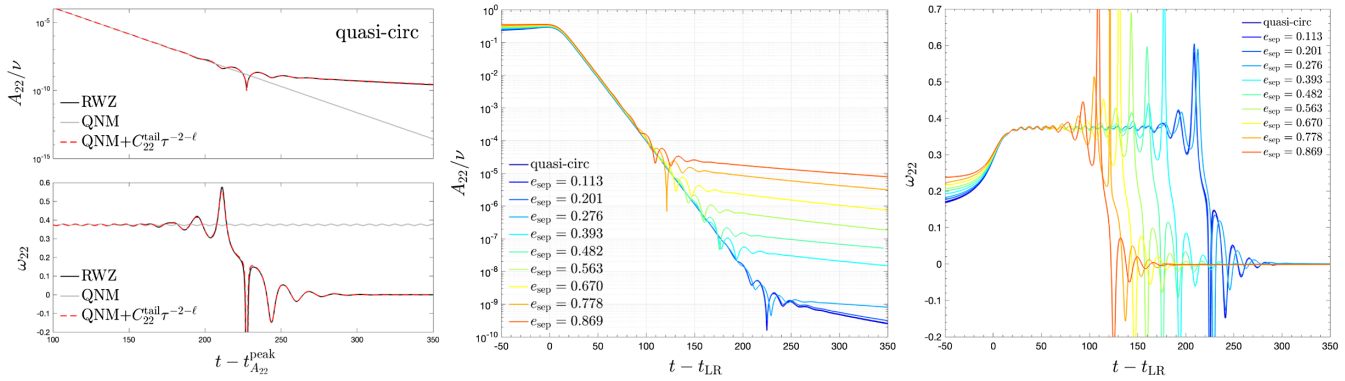

FIG. 19. Leftmost panel: Amplitude and frequency of the Zerilli (2,2) of the quasicircular waveform (black) compared with the results obtained considering only the QNMs contribution (gray) and the QNMs plus tail (dashed red). Middle and rightmost: RWZ amplitudes and frequencies for different eccentricities, aligned with respect to the light-ring crossing.

and $-2-\ell$ is the asymptotic behavior of the tail term at future null infinity [62]. Using the (fundamental) QNMs and the power-law tail we can fully catch the behavior of the numerical amplitude and frequency, as shown in the left panel of Fig. 19. When eccentricity is taken into account, the tail contribution becomes more significant and starts to dominate over the QNM decay earlier, as shown in the middle and right panels of Fig. 19. Moreover, the tail cannot be described as before using the ansatz $C_{22}^{\rm tail}\tau^{-2-\ell}$ since the tail has not reached yet the asymptotic behavior. For example, for the configuration with $e_0=0.5$ the decay-rate is roughly -1.3 instead of $-2-\ell$. Similar numbers are obtained for the other eccentric configurations with $e\gtrsim 0.3$.

VI. HEURISTIC MODELING OF QNMs EXCITATION

Let us now introduce a toy model to grasp some insights on how the excitation of QNMs is driven by the dynamics and the related presence of a source term in the right hand side of the RWZ equations. Following Ref. [13], and in particular Sec. III B, we base our analysis on the understanding that a Schwarzschild black hole can be seen as a resonating object. We start by generalizing Eq. (8), assuming that the constant coefficients $C^{\pm}_{\ell mn}$ are instead time-dependent functions, $C^{\pm}_{\ell mn}(t)$. The ringdown waveform reads then

$$\Psi^{(\mathrm{o/e})}_{\ell m}=\sum_n \Psi^{(\mathrm{o/e})}_{\ell mn}, \tag{45}$$

$$\Psi^{(\mathrm{o/e})}_{\ell mn}(t)\equiv C^{+}_{\ell mn}(t)e^{-\sigma^{+}_{\ell n}t}+C^{-}_{\ell mn}(t)e^{-\sigma^{-}_{\ell n}t}. \tag{46}$$

Here the origin of time, $t=0$, is assumed to be the light-ring crossing, $t_{\rm LR}$. The final goal of our investigation is to determine an approximate semianalytical expression for the coefficients $C^{\pm}_{\ell mn}(t)$ so to understand when the associated QNMs are excited. Since we know that the solution of the homogeneous RWZ equations is a superposition of QNMs with constant coefficients $C^{\pm}_{\ell mn}$, each spherical mode is thought as as the solution of the homogeneous second order differential equation

$$\ddot{\Psi}^{(\mathrm{o/e})}_{\ell mn}+2\alpha_{\ell n}\dot{\Psi}^{(\mathrm{o/e})}_{\ell mn}+(\alpha^2_{\ell n}+\omega^2_{\ell n})\Psi^{(\mathrm{o/e})}_{\ell mn}=0, \tag{47}$$

under the ansatz $\Psi_{\ell mn}(t)\propto e^{-\sigma^{\pm}_{\ell n}t}$, with $\sigma^{\pm}_{\ell n}=\alpha_{\ell n}\pm i\omega_{\ell n}$. This is indeed the equation of an underdamped oscillator with damping coefficient $\alpha_{\ell n}$ and undamped angular frequency $\pm\omega_{\ell n}$. An external force $F(t)$ in the right-hand side of Eq. (47) yields an inhomogeneous differential equation corresponding to a driven harmonic oscillator. Our model is thus defined by *assuming* that the forcing term is given by Eq. (42), that is $F(t)\equiv F^{(\mathrm{o/e})}_{\ell m}(t)$. The solution of this inhomogeneous equation can be obtained starting from the one of the homogeneous problem by promoting the numerical coefficients therein to time-dependent functions. This is referred to as the *method of variation of parameters* (or *method of osculating elements*) [63–65]. With this approach we know *a priori* that the differential equation

$$\ddot{\Psi}^{(\mathrm{o/e})}_{\ell mn}+2\alpha_{\ell n}\dot{\Psi}^{(\mathrm{o/e})}_{\ell mn}+(\alpha^2_{\ell n}+\omega^2_{\ell n})\Psi^{(\mathrm{o/e})}_{\ell mn}=F^{(\mathrm{o/e})}_{\ell m}(t) \tag{48}$$

admits a solution with the precise QNM structure of Eq. (46). We start by writing the time derivative of our particular solution *as if* the coefficients $C^{\pm}_{\ell mn}(t)$ were not time-dependent. This is equivalent to impose

$$\dot{\Psi}^{(\mathrm{o/e})}_{\ell mn}(t)=-\sigma^{+}_{\ell n}C^{+}_{\ell mn}(t)e^{-\sigma^{+}_{\ell n}t}-\sigma^{-}_{\ell n}C^{-}_{\ell mn}(t)e^{-\sigma^{-}_{\ell n}t}, \tag{49}$$

which is true only if the time dependence of $C^{\pm}_{\ell mn}(t)$ gives no contribution to the time derivative, namely if the condition

$$\dot{C}^{+}_{\ell mn}(t)e^{-\sigma^{+}_{\ell n}t}+\dot{C}^{-}_{\ell mn}(t)e^{-\sigma^{-}_{\ell n}t}=0 \tag{50}$$

is satisfied. We can then take another time derivative on Eq. (49) in order to obtain $\ddot{\Psi}^{(\mathrm{o/e})}_{\ell m}$. We then insert $\dot{\Psi}^{(\mathrm{o/e})}_{\ell m}$ and $\ddot{\Psi}^{(\mathrm{o/e})}_{\ell m}$ in Eq. (48) and, considering that the sum of all the terms without the time derivatives $\dot{C}^{\pm}_{\ell mn}(t)$ separately solves the associated homogeneous equation (47), we get the second condition

$$-\sigma^{+}_{\ell n}\dot{C}^{+}_{\ell mn}(t)e^{-\sigma^{+}_{\ell n}t}-\sigma^{-}_{\ell n}\dot{C}^{-}_{\ell mn}(t)e^{-\sigma^{-}_{\ell n}t}=F^{(\mathrm{e/o})}_{\ell m}(t), \tag{51}$$

which together with Eq. (50) builds up a system of two equations that can be solved for $\dot{C}^{\pm}_{\ell mn}(t)$. A straightforward computation yields

$$\dot{C}^{\pm}_{\ell mn}(t)=\pm i\frac{e^{\sigma^{\pm}_{\ell n}t}F^{(\mathrm{e/o})}_{\ell m}(t)}{2\omega_{\ell n}}, \tag{52}$$

and an ensuing time integral gives us the final expressions

$$C^{\pm}_{\ell mn}(t)=C^{\pm}_{\ell mn}(t_0)\pm\frac{i}{2\omega_{\ell n}}\int_{t_0}^{t}dt' F^{(\mathrm{e/o})}_{\ell m}(t')e^{\sigma^{\pm}_{\ell n}t'}, \tag{53}$$

where t_0 is an arbitrary initial time. Considering that $F^{(\mathrm{e/o})}_{\ell m}(t')$ does not diverge during the inspiral and that in the integrand we have $e^{\sigma^{\pm}_{\ell n}t'}$, we have that the computation of $C^{\pm}_{\ell mn}(t)$ is not influenced by the choice of t_0 as long as t_0 is not too close to $t_{\rm LR}$. In practice, we start to integrate from the beginning of our simulation.

A. Results

Some results for the (2,2) and (2,1) multipoles are shown in Fig. 20. In the leftmost panel we show the absolute value

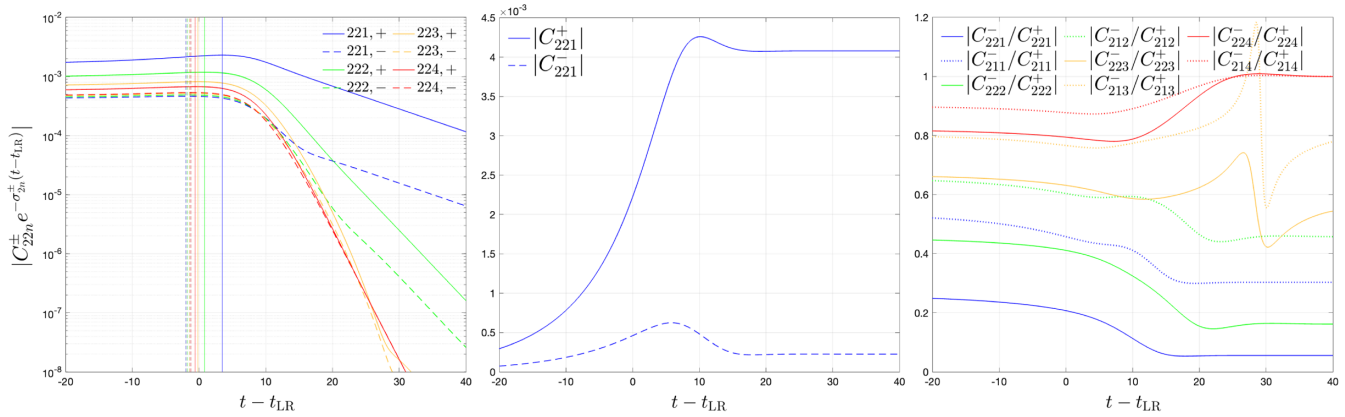

FIG. 20. Time-dependent QNM-excitation coefficients $C^{\pm}_{\ell mn}(t)$ for the quasicircular case, see Eq. (53). The positive-frequency modes are more relevant and are excited later than the negative ones, as shown by the location of the amplitude maxima (vertical lines in the leftmost plot). In the middle panel we plot the activationlike excitation coefficients for the fundamental frequency. The rightmost panel highlights the hierarchy of the ratios $|C^{-}_{\ell mn}/C^{+}_{\ell mn}|$ for the overtones of the (2,2) and (2,1) multipoles. Note that the beating is more relevant for the (2,1) mode (dotted line) than for the quadrupole (solid lines).

of the positive and negative parts of the solution, $|C^{\pm}_{\ell mn}(t)e^{-\sigma^{\pm}_{\ell n}(t-t_{\rm LR})}|$, for $n \leq 4$. We see that the negative-frequency contributions are smaller than the corresponding positive ones. The model thus predicts the negative-frequency modes to be less excited than the positive ones. The same feature can be seen in the third plot of the same figure, where we show the absolute value of the ratios of negative and positive solutions. In addition (see the rightmost panel of the figure) the negative-frequency modes become more and more relevant as n grows. This behavior is consistent with the qualitative discussion of Ref. [13], see in particular Fig. 4. In that case, the authors argued that the positive QNMs are excited during the plunge since the Newtonian frequency of the waveform $m\Omega$ gets "closer" to the positive QNM frequencies. Note in addition that what is found here is consistent with the structure of the actual solution of the RWZ equation. The second interesting finding, illustrated by the middle panel of Fig. 20, is that $|C^{\pm}_{\ell m1}(t)|$ is reminiscent of an activation function and becomes constant after $t \sim t_{\rm LR} + 15$, showing that from that time onward the $n = 1$ solution can be written as a superposition of QNMs with constant coefficients. For the first overtone, we have that $C^{\pm}_{\ell m2}(t)$ has a similar behavior. However, for the $n \geq 3$ overtones, the behavior of $C^{\pm}_{\ell mn}(t)$ is less reminiscent of an activation function. In particular, for $n = 3$ we see some oscillations in the solution, as can be seen, e.g., from the third panel of Fig. 20. We are prone to exclude that these are physical features that can be found also in the full-RWZ case, and we rather interpret them as expressions of the limitation of our toy model. The third consideration regards the values of the $|C^{-}_{\ell mn}(t)/C^{+}_{\ell mn}(t)|$ ratios for different multipoles. We show these ratios for the (2,2) and (2,1) multipoles in the third panel of Fig. 20 with solid and dotted lines, respectively. As can be seen, the ratios of the (2,1) multipole are higher than the ones of the (2,2) multipole for the same n. This means that, according to our toy model, the mode mixing in the (2,1) multipole should be more evident than in the (2,2). This is precisely what happens in the numerical solutions of the full RWZ equations, as shown in Table III. The driven harmonic oscillator correctly predict also the qualitative relevance of the mode-mixing in the (3,3) multipole, since the predicted ratio $|C^{-}_{331}(t)/C^{+}_{331}(t)|$ is smaller than the one of the (2,2) mode and, as can be seen from the numerical data, the mode-mixing is more relevant in the (2,2) multipole rather than in the (3,3). The final interesting feature that we discuss is that the positive and negative solutions reach their peaks at different times. This is shown for the (2,2) multipole in the first plot, where we mark the peak-times with vertical lines (solid for positive-frequency modes and dashed for negative ones). As can be seen, the negative modes with same n are excited before the corresponding positive modes, and the overtones are excited before the fundamental QNMs.

To conclude, with this toy model we have reproduced some features that are observed when solving the actual RWZ equations and we have also argued that the overtones are excited before the fundamental frequency. However, since these results are only qualitative, we cannot exploit them to improve the description of the postpeak waveform.

VII. CONCLUSIONS

The results of this paper are twofold: (i) on the one hand, it is studied the transition from eccentric inspiral to plunge, merger and ringdown of a binary black hole coalescence in the large mass ratio limit (or particle limit) and its gravitational wave emission; (ii) on the other hand, it is introduced and tested an EOB waveform valid in this limit. This improves previous results [13] and generalizes them to the eccentric case, that was not studied systematically

so far. Since the large mass ratio limit can be seen as a well-controlled theoretical laboratory to learn and explore new ideas, this work should be seen as part of the currently ongoing effort of building accurate waveform templates for eccentric (comparable-mass) binaries within the EOB formalism [6,43,66–70]. More in detail, our results can be summarized as follows:

(i) We performed a systematic survey of eccentric nonspinning binaries in the test particle limit, focusing in particular on the transition from inspiral to plunge and on the phenomenology of the corresponding waveform, computed solving numerically the RWZ equations, Eq. (6), with the RWZhyp code [16,40,41].

(ii) We discussed a new ringdown model for eccentric binaries in the test particle limit, modifying the primary fitting templates used in previous works [20,42]. Notably, the ringdown model includes the mode-mixing between positive and negative frequency fundamental QNMs. The global fits on the parameter space are performed using as fitting parameter the gauge-invariant quantity $\hat{b}_{\Omega_{\rm pk}}$ [Eq. (17)], that is defined as the ratio between the angular momentum and energy at the peak of the orbital frequency (i.e., at the light-ring crossing). This moment can be considered a good definition of the merger time within our context.

(iii) We then built a complete test-mass EOB model for eccentric nonspinning binaries, including also higher modes and 2PN noncircular corrections in the $\ell = m = 2$ waveform mode. We analyzed in details the impact of several analytical building blocks, in particular we tested: (i) the relevance of the generic Newtonian prefactor, also in the quasicircular case, (ii) the contribution of the 2PN noncircular corrections introduced in Refs. [47–49], (iii) different prescriptions for the NQC corrections, and in particular the point at which they are computed; (iv) the ringdown attachment point. All these ingredients together provide an accurate complete EOB waveform, yielding $\Delta\phi_{22} \lesssim 0.01$ rad in the quasicircular case, and $\Delta\phi_{22} \lesssim 0.05$ rad during the merger-ringdown for all the eccentric configurations considered. Building upon methods introduced in the SEOBNR-family [53,55,56], we also explored the performance of a different ringdown model for the higher modes that starts from $t^{\rm peak}_{A_{22}}$ rather than from $t^{\rm peak}_{A_{\ell m}}$.

(iv) We analyzed the build-up of QNMs excitation, revisiting also the matching comb procedure that was used in former EOB models [13,52,59,71,72]. Within this context, we also introduced a heuristic model to compute the excitation coefficients of the QNMs in the presence of a driving source. The results of this model are in qualitatively and semiquantitative agreement with the actual structure of the waveform. We also discussed how the power-law tail contribution presents at the end of the ringdown changes in the presence of eccentricity.

ACKNOWLEDGMENTS

S. A. and A. P. acknowledge the stimulating environment of IHES, were part of this research was conducted. In particular, it was partly supported by the *"2021 Balzan Prize for Gravitation: Physical and Astrophysical Aspects"*, awarded to Thibault Damour. We are also grateful to D. Chiaramello for producing most of the nonspinning simulations discussed in this work. S. B. acknowledges support by the EU H2020 under ERC Starting Grant No. BinGraSp-714626 and by the EU Horizon under ERC Consolidator Grant No. InspiReM-101043372. S. A. is grateful to Tilly Gatto and Stefano Belisari for continuous support during the development of this work. We are also grateful to P. Micca for, never trivial, inspiring suggestions.

APPENDIX A: REGRIDDING USED FOR NQC CORRECTIONS DETERMINATION AND MATCHING

As anticipated in Sec. III B and Sec. III C, the fact that the dynamics is obtained solving the Hamilton's equations (1) numerically with an ODE solver implies that we have a discrete time array. All the dynamical quantities and the waveform are thus computed on this array. This discretization can lead to issues when matching the inspiral waveform to the ringdown.

The first issue of this kind is related to the NQC corrections determination. Indeed, in order to determine the coefficients a_i and b_i of Eq. (23), we have to solve the linear system (25). However, the rhs is computed exactly at $t^{\rm NQC}_{\ell m}$ (since if $t^{\rm NQC}_{\ell m} > t^{\rm peak}_{A_{\ell m}}$ we compute it from the analytical ringdown waveform discussed in Sec. II C, while if $t^{\rm NQC}_{\ell m} < t^{\rm peak}_{A_{\ell m}}$ we extract it at $t^{\rm NQC}_{\ell m}$ using a cubic spline procedure on the numerical data), but the lhs is not. The latter is indeed evaluated using the inspiral waveform $h^{\rm inspl}_{\ell m}$, that is in turn computed from the EOB dynamics, which is found solving the Hamilton's equation with a discrete-step ODE-solver. Therefore, $t^{\rm NQC}_{\ell m}$ is not guaranteed to be a point of the time array on which the inspiral waveform is computed. This implies that the lhs and the rhs might be computed at slightly different times and this can introduce a systematic error in the computation of the NQC coefficients a_i and b_i, and thus in the complete EOB waveform. The second issue is related to the matching procedure. Indeed, in order to match the NQC-corrected inspiral-plunge waveform to the ringdown model we need to compute $\phi^{\rm peak}_{\ell m}$, i.e., the phase of the inspiral-plunge waveform at the matching-point, see Eq. (9). However, it is not guaranteed that the

matching time $t^{\rm peak}_{A_{\ell m}}$ is an element of the time array used to compute the dynamics. If we operate without performing a regrid, the phase $\phi^{\rm peak}_{\ell m}$ found can be flawed.

In order to solve the aforementioned issues, we apply for each multipole a regridding procedure in the vicinity of $t^{\rm NQC}_{\ell m}$ and $t^{\rm peak}_{A_{\ell m}}$, so that these two points are enforced to be elements of the time grid. We then interpolate the chunks of the waveform that we need on the refined time arrays using a cubic spline algorithm. We then compute the NQC coefficients, a_i and b_i, and we perform the match between the inspiral-plunge waveform and the ringdown model on the refined time grid where $t^{\rm peak}_{A_{\ell m}}$ is a grid-point. We prefer to reinterpolate the obtained waveform back on the original time array used to solve the Hamilton's equations in order to have a uniform time step, but note that this step is not necessary. The results for different regridding configurations are shown in Fig. 21 We consider the analytical waveform without regridding (solid yellow), the one with regridding only for the NQC corrections (dash-dotted blue), the one with regridding only for the matching procedure (dashed green) and the one with regridding in both the NQC corrections and matching (dotted red). The latter is the default option and it is also the one shown in Fig. 7. As can be seen from the middle panel, for the amplitude the most relevant regridding is the one associated to the matching, while the one associated to the NQC does not seem important. The regridding in the matching zone drives the relative amplitude difference in the late ringdown from the 2.3% to be below the 0.1%. For the phase, which analytical/numerical difference is shown in the third panel, we have that both regriddings are important. Indeed, if we do not consider any regridding, the analytical/numerical phase difference during the ringdown is about -0.05 radians, while with the full regridding procedure the phase difference drops of one order of magnitude, reaching -0.006 radians.

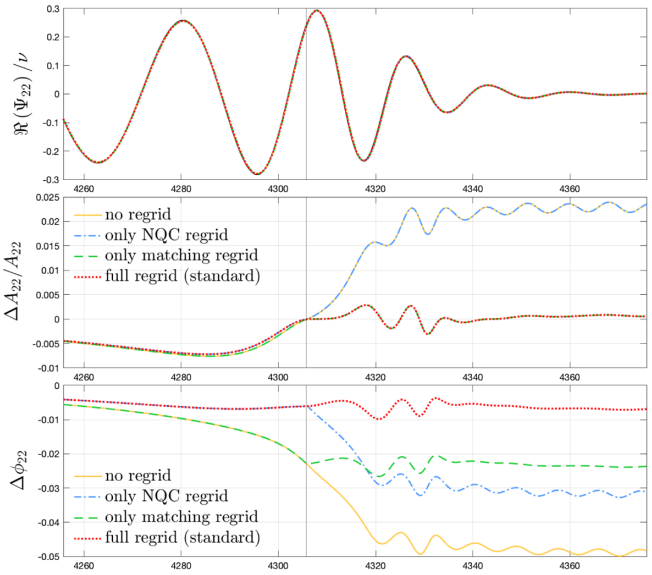

FIG. 21. Analytical/numerical comparison for the (2,2) waveform multipole considering different regridding configurations. In the top panel we show the RWZ numerical waveform (black, almost indistinguishable) and the analytical ones using different colors. See legend and text for more details. Note that the red analytical (2,2) waveform is the standard one, i.e., the one shown in Fig. 7. In the middle and bottom panels we show the relative amplitude difference and the phase difference in radians, with same color scheme. The vertical black line marks the peak of A_{22}.

APPENDIX B: TIME-DOMAIN FITS OF THE POSTPEAK WAVEFORM USING QNMs

In this appendix we attempt to fit the complete postpeak waveform using the pure QNMs ansatz of Eq. (8) on a time interval $\tau \equiv t - t^{\rm peak}_{A_{22}} \in [t^{\rm QNM}_0, 100]$. We start by performing the fit of the real and imaginary parts of the waveform using the fundamental QNMs and 7 overtones starting from the peak of the amplitude, i.e., considering $n = 8$ and $t^{\rm QNM}_0 = 0$; the results of this procedure are shown in Fig. 22 (dash-dotted green lines). The QNMs waveform overlaps quite well with the numerical RWZ waveform (black), and the corresponding residual is around 10^{-3} shortly after the amplitude peak. However, it is easy to see that (i) the beating between positive and negative frequency QNMs in the late ringdown is not well reproduced, as shown by the waveform frequency in the second panel, (ii) the frequency of the fitted wave shows spurious oscillations in the early ringdown. In order to ensure the correct late-ringdown behavior, we refine this procedure by prefitting only the fundamental QNMs on $\tau \in [62, 100]$, so that we can easily find $C^{\pm}_{221}$ since the overtones are negligible in the late ringdown, and then performing the fit of Eq. (8) on the whole time interval $\tau \in [0, 100]$, so that we can find the remaining $C^{\pm}_{\ell mn}$ coefficients. The result of this procedure is shown with dashed red lines in Fig. 22. While the beating in the late ringdown frequency is now well reproduced, the spurious oscillations in the early ringdown frequency are still present. Note that in this case the residual is a little bit higher in the early ringdown, but way lower in the late evolution. We thus concluded that, while the residual of the waveforms in quite low in both fits, the waveform frequency shows that there are some inaccuracies in the early ringdown.

In an attempt to solve the issue of the spurious frequency oscillations, we also explore the possibility to find the $C^{\pm}_{\ell mn}$ coefficients fitting directly the frequency using Eq. (43). Note that if we proceed this way, we cannot find C^{+}_{221} since the frequency is invariant under global normalizations and phase shifts of the waveform. We thus find C^{+}_{221} as done before, i.e., fitting Eq (8) with $n = 1$ in the late time interval $\tau \in [62, 100]$. In the left panel of Fig. 23 we show this frequency fit compared with the waveform fit discussed above. To evaluate the goodness of the fits, we show in this

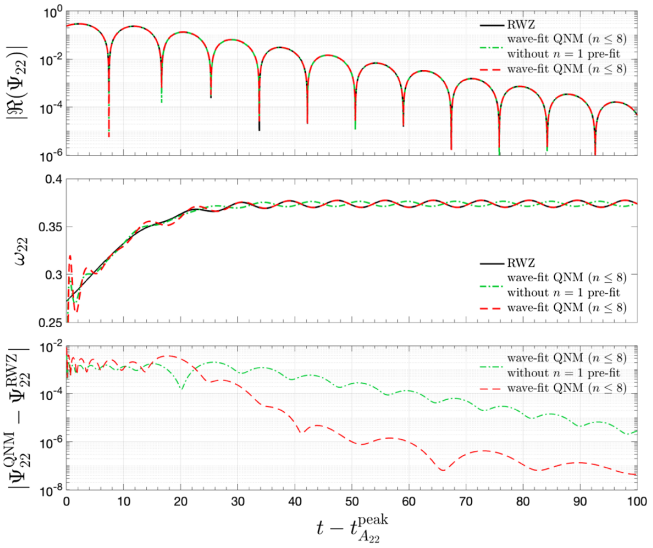

FIG. 22. Upper panels: RWZ waveform and frequency (black) compared with the results from the waveform fits performed (1) considering all the QNMs together (dash-dotted green), and (2) prefitting the fundamental QNMs (dashed red) and then fitting all the overtones. In the bottom panel we show the residuals with same color scheme. See discussion in Appendix B.

case the relative differences of amplitude and frequency, that we consider more informative than the residual. As can be seen, while the frequency fit solves the issue of the early spurious oscillations, produce a waveform that is way less accurate than the one found with the waveform fit.

Finally, in the right panels of Fig. 23 we show the comparison between the frequency and waveform fits performed considering $n = 4$ and $t_0^{\rm QNM} = 15$. In this case the waveform fit is accurate and the recovered frequency is consistent with the numerical result, leading to relative amplitude and frequency errors around 10^{-4}. However, the amplitude of the waveform recovered from the frequency fit reaches a 10% error at $\tau \sim 15$, and thus the frequency fit seems less robust than the waveform fit, even if we do not fit the early ringdown.

We thus conclude that (i) it is a good practice to check the waveform frequency in order to evaluate the goodness of the QNMs fits of the ringdown waveform, (ii) the waveform can be consistently fitted, but only starting from later times. This is again consistent with the discussion of Sec. V A on the RWZ source terms and with the iterative frequency fit of Sec. V B.

APPENDIX C: GLOBAL FITS

In this appendix we report all the global fits that we use in our model, see Sec. II E for a general discussion on how we perform the global fits. We start by reporting the global fits of the quantities needed to reconstruct the postpeak waveform for all the modes in Tables V and VI, see definitions in Sec. II C. We then proceed to show the global fits for $\{A_{22}^{\rm NQC}, \dot{A}_{22}^{\rm NQC}, \ddot{A}_{22}^{\rm NQC}, \omega_{22}^{\rm NQC}, \dot{\omega}_{22}^{\rm NQC}, \ddot{\omega}_{22}^{\rm NQC}\}$ evaluated at $t_{\ell m}^{\rm NQC} = t_{A_{\ell m}}^{\rm peak} - 2$ in Tables VII and VIII. Note that we report the fits also for $\ell = m = 2$, but for the quadrupolar waveform we do not use them since we use $t_{22}^{\rm NQC} = t_{A_{22}}^{\rm peak} + 2$, see Sec. III B for discussion. Note that in all the cases we use a parabolic global template.

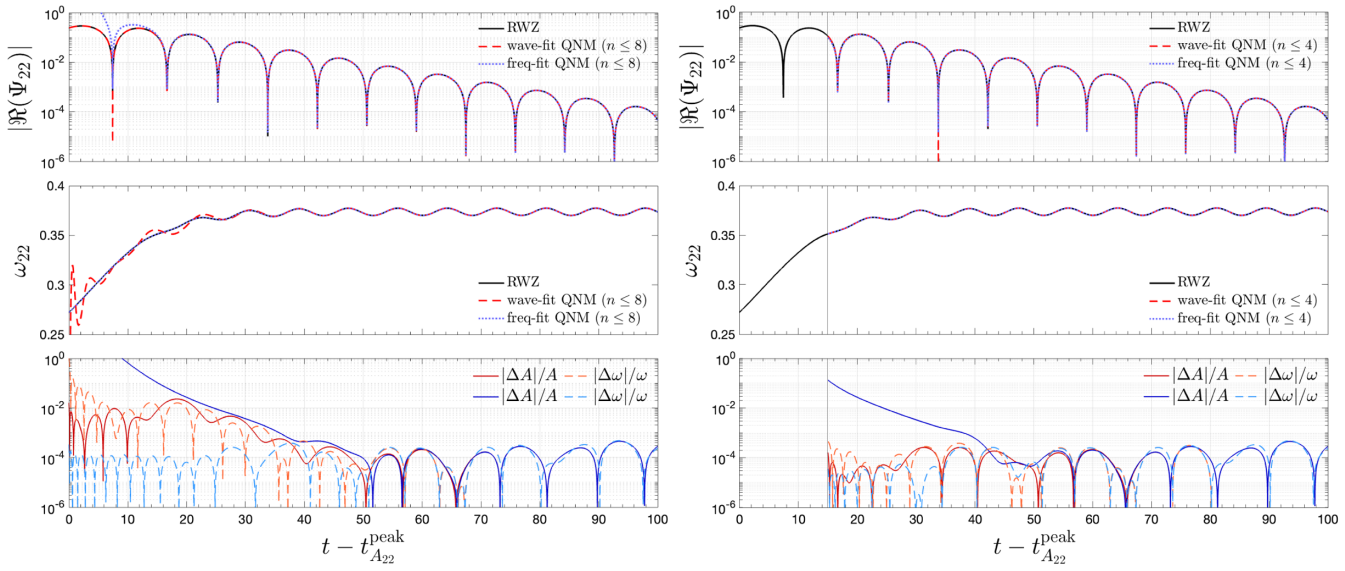

FIG. 23. Upper panels: RWZ waveform and frequency (black) compared with the results from the wave fit (red) and frequency fit (blue). In the bottom panels we show the relative differences of the amplitude and frequency (hot colors for the waveform fit, cold colors for the frequency fit). On the left, we fit the whole postpeak waveform using 8 QNMs, while on the right we fit from $t \geq 15 + t_{A_{22}}^{\rm peak}$ using 4 QNMs. See discussion in Appendix B.

TABLE V. Global fits of the coefficients entering the ringdown template. For each quantity y, the fitting function is: $y = C_{\rm QC} + C_1 \hat{b}_{\Omega_{\rm pk}} + C_2 \hat{b}^2_{\Omega_{\rm pk}}$, where QC indicates the quasicircular value. The amplitude considered in this table is the amplitude of the strain, $A_{\ell m} = |h_{\ell m}|$, rather than the amplitude of the RWZ-normalized waveform.

(ℓ, m)	Coefficient	$C_{\rm QC}$	C_1	C_2
(2,2)	c_2^ϕ	1.561×10^{-1}	-5.067×10^{-2}	-5.493×10^{-2}
	c_3^ϕ	3.272	5.021	6.554
	c_4^ϕ	2.592	8.305	1.108×10^{2}
	c_2^A	2.161×10^{-1}	-1.999×10^{-2}	7.199×10^{-3}
	c_3^A	2.334	3.030	5.583
	$A_{\rm peak}$	1.444	9.914×10^{-1}	9.177×10^{-1}
	$\ddot{A}_{\rm peak}$	-2.359×10^{-3}	6.830×10^{-3}	-3.238×10^{-3}
	$\Delta\omega_{\rm peak}$	1.015×10^{-1}	-1.061×10^{-2}	4.131×10^{-3}
(2,1)	c_2^ϕ	1.539×10^{-1}	4.563×10^{-2}	1.250×10^{-1}
	c_3^ϕ	1.185	1.721	10.167
	c_4^ϕ	3.866	7.989	80.460
	c_2^A	3.656×10^{-1}	2.191×10^{-1}	-2.017
	c_3^A	-1.535×10^{-1}	-3.204	31.896
	$A_{\rm peak}$	5.238×10^{-1}	2.332×10^{-1}	2.119×10^{-1}
	$\ddot{A}_{\rm peak}$	-2.624×10^{-3}	5.624×10^{-3}	2.423×10^{-2}
	$\Delta\omega_{\rm peak}$	8.302×10^{-2}	-8.936×10^{-2}	5.023×10^{-1}
(3,3)	c_2^ϕ	1.783×10^{-1}	-1.361×10^{-2}	-1.330×10^{-3}
	c_3^ϕ	2.818	4.107	9.523
	c_4^ϕ	1.536	4.592	28.099
	c_2^A	2.192×10^{-1}	-1.750×10^{-2}	3.036×10^{-2}
	c_3^A	1.585	1.715	2.634
	$A_{\rm peak}$	5.635×10^{-1}	4.299×10^{-1}	3.883×10^{-1}
	$\ddot{A}_{\rm peak}$	-1.823×10^{-3}	2.287×10^{-3}	1.026×10^{-3}
	$\Delta\omega_{\rm peak}$	1.462×10^{-1}	-1.916×10^{-2}	1.800×10^{-2}
(3,2)	c_2^ϕ	1.851×10^{-1}	-8.128×10^{-3}	9.774×10^{-3}
	c_3^ϕ	1.308	3.395×10^{-1}	7.985×10^{-1}
	c_4^ϕ	2.172×10^{-1}	1.135×10^{-1}	2.334×10^{-1}
	c_2^A	2.425×10^{-1}	6.597×10^{-4}	-7.605×10^{-3}
	c_3^A	9.188×10^{-1}	8.761×10^{-1}	-4.018×10^{-1}
	$A_{\rm peak}$	1.991×10^{-1}	1.289×10^{-1}	1.017×10^{-1}
	$\ddot{A}_{\rm peak}$	-1.561×10^{-3}	-5.955×10^{-4}	6.250×10^{-4}
	$\Delta\omega_{\rm peak}$	1.476×10^{-1}	1.704×10^{-4}	9.627×10^{-3}
(3,1)	c_2^ϕ	1.483×10^{-1}	-7.316×10^{-3}	2.289×10^{-2}
	c_3^ϕ	1.406×10^{-4}	-2.424×10^{-4}	6.491×10^{-4}
	c_4^ϕ	6.005×10^{-5}	-4.839×10^{-5}	1.522×10^{-4}
	c_2^A	2.917×10^{-1}	-1.330×10^{-1}	2.315×10^{-1}
	c_3^A	2.068	-1.589	2.079
	$A_{\rm peak}$	6.230×10^{-2}	2.460×10^{-2}	1.575×10^{-2}
	$\ddot{A}_{\rm peak}$	-2.678×10^{-3}	-1.660×10^{-3}	5.739×10^{-4}
	$\Delta\omega_{\rm peak}$	1.881×10^{-1}	-3.904×10^{-2}	1.385×10^{-2}

TABLE VI. Global fits of the coefficients entering the ringdown template. For each quantity y, the fitting function is: $y = C_{\rm QC} + C_1 \hat{b}_{\Omega_{\rm pk}} + C_2 \hat{b}^2_{\Omega_{\rm pk}}$, where QC indicates the quasicircular value. The amplitude considered in this table is the amplitude of the strain, $A_{\ell m} = |h_{\ell m}|$, rather than the amplitude of the RWZ-normalized waveform.

(ℓ, m)	Coefficient	$C_{\rm QC}$	C_1	C_2
(4,4)	c_2^ϕ	1.845×10^{-1}	-6.271×10^{-3}	-2.849×10^{-3}
	c_3^ϕ	2.249	2.991	5.909
	c_4^ϕ	1.025	2.617	12.471
	c_2^A	2.178×10^{-1}	-1.276×10^{-2}	2.823×10^{-2}
	c_3^A	1.145	1.476	2.040
	$A_{\rm peak}$	2.754×10^{-1}	2.374×10^{-1}	2.296×10^{-1}
	$\ddot{A}_{\rm peak}$	-1.258×10^{-3}	8.999×10^{-4}	8.471×10^{-4}
	$\Delta\omega_{\rm peak}$	1.751×10^{-1}	-1.720×10^{-2}	1.743×10^{-2}
(4,3)	c_2^ϕ	1.876×10^{-1}	-2.091×10^{-3}	2.781×10^{-4}
	c_3^ϕ	1.320	1.129	-7.914×10^{-4}
	c_4^ϕ	3.513×10^{-1}	6.880×10^{-1}	3.418×10^{-1}
	c_2^A	2.252×10^{-1}	4.376×10^{-3}	-6.836×10^{-2}
	c_3^A	3.600×10^{-1}	1.192	-3.611
	$A_{\rm peak}$	9.418×10^{-2}	7.365×10^{-2}	6.538×10^{-2}
	$\ddot{A}_{\rm peak}$	-7.851×10^{-4}	-4.334×10^{-5}	-1.645×10^{-4}
	$\Delta\omega_{\rm peak}$	1.722×10^{-1}	8.015×10^{-3}	-2.205×10^{-2}
(4,2)	c_2^ϕ	1.848×10^{-1}	-1.045×10^{-2}	2.014×10^{-2}
	c_3^ϕ	1.316	4.910×10^{-1}	-3.244×10^{-1}
	c_4^ϕ	8.103×10^{-1}	1.244	-1.645
	c_2^A	2.589×10^{-1}	4.823×10^{-2}	-1.436×10^{-1}
	c_3^A	-7.454×10^{-1}	1.157	-1.954
	$A_{\rm peak}$	3.138×10^{-2}	1.544×10^{-2}	1.181×10^{-2}
	$\ddot{A}_{\rm peak}$	-2.743×10^{-4}	1.623×10^{-4}	-3.799×10^{-4}
	$\Delta\omega_{\rm peak}$	1.836×10^{-1}	-2.595×10^{-2}	2.780×10^{-2}
(4,1)	c_2^ϕ	1.428×10^{-1}	-1.797×10^{-2}	3.577×10^{-2}
	c_3^ϕ	-7.583×10^{-1}	-3.777×10^{-1}	6.408×10^{-1}
	c_4^ϕ	1.155×10^{-1}	1.294×10^{-1}	-2.141×10^{-1}
	c_2^A	1.067	-4.888×10^{-1}	8.161×10^{-1}
	c_3^A	10.890	-4.684	8.425
	$A_{\rm peak}$	9.263×10^{-3}	3.514×10^{-3}	2.333×10^{-3}
	$\ddot{A}_{\rm peak}$	-7.568×10^{-4}	-4.506×10^{-4}	-3.366×10^{-5}
	$\Delta\omega_{\rm peak}$	2.572×10^{-1}	-5.064×10^{-2}	6.728×10^{-2}
(5,5)	c_2^ϕ	1.872×10^{-1}	-3.773×10^{-3}	-1.675×10^{-3}
	c_3^ϕ	1.844	2.360	3.290
	c_4^ϕ	7.272×10^{-1}	1.786	5.737
	c_2^A	2.157×10^{-1}	-6.055×10^{-3}	-7.261×10^{-3}
	c_3^A	8.165×10^{-1}	1.536	3.433×10^{-1}
	$A_{\rm peak}$	1.509×10^{-1}	1.458×10^{-1}	1.537×10^{-1}
	$\ddot{A}_{\rm peak}$	-8.648×10^{-4}	3.099×10^{-4}	4.012×10^{-4}
	$\Delta\omega_{\rm peak}$	1.954×10^{-1}	-1.188×10^{-2}	-5.822×10^{-3}

TABLE VII. Global fits of the coefficients for the quantities used to determine NQC corrections for $t^{\rm NQC}_{\ell m} = t^{\rm peak}_{A_{\ell m}} - 2$. The fitting template is a quadratic function: $y = C_{\rm QC} + C_1 \hat{b}_{\Omega_{\rm pk}} + C_2 \hat{b}^2_{\Omega_{\rm pk}}$. The amplitude considered in this table is RWZ-normalized as usual, i.e. $A_{\ell m} = |\Psi_{\ell m}| = |h_{\ell m}|/\sqrt{(\ell+2)(\ell+1)\ell(\ell-1)}$.

(ℓ, m)	$X^{\rm NQC}_{\ell m}$	$C_{\rm QC}$	C_1	C_2
(2,2)	A	2.938×10^{-1}	2.049×10^{-1}	1.860×10^{-1}
	$\dot{A}$	7.898×10^{-4}	-2.420×10^{-3}	1.338×10^{-3}
	$\ddot{A}$	-3.160×10^{-4}	1.042×10^{-3}	-7.056×10^{-4}
	ω	2.609×10^{-1}	3.121×10^{-2}	-2.361×10^{-3}
	$\dot{\omega}$	5.367×10^{-3}	-1.031×10^{-2}	-5.196×10^{-4}
	$\ddot{\omega}$	2.649×10^{-4}	1.256×10^{-4}	-1.332×10^{-3}
(2,1)	A	1.063×10^{-1}	5.236×10^{-2}	2.594×10^{-2}
	$\dot{A}$	4.784×10^{-4}	-1.940×10^{-3}	1.196×10^{-3}
	$\ddot{A}$	-1.140×10^{-4}	4.152×10^{-4}	-3.622×10^{-3}
	ω	2.809×10^{-1}	2.037×10^{-2}	-1.893×10^{-1}
	$\dot{\omega}$	9.270×10^{-3}	7.587×10^{-3}	3.664×10^{-2}
	$\ddot{\omega}$	-3.868×10^{-3}	9.083×10^{-4}	3.541×10^{-2}
(3,3)	A	5.115×10^{-2}	3.967×10^{-2}	3.547×10^{-2}
	$\dot{A}$	2.767×10^{-4}	-4.255×10^{-4}	1.457×10^{-5}
	$\ddot{A}$	-1.109×10^{-4}	1.999×10^{-4}	-5.411×10^{-5}
	ω	4.322×10^{-1}	4.023×10^{-2}	-2.155×10^{-3}
	$\dot{\omega}$	1.026×10^{-2}	-1.279×10^{-2}	3.809×10^{-4}
	$\ddot{\omega}$	3.777×10^{-4}	5.998×10^{-4}	-1.296×10^{-3}
(3,2)	A	1.790×10^{-2}	1.174×10^{-2}	9.344×10^{-3}
	$\dot{A}$	2.582×10^{-4}	-3.442×10^{-7}	-3.865×10^{-5}
	$\ddot{A}$	-1.076×10^{-4}	4.345×10^{-5}	-2.468×10^{-5}
	ω	4.205×10^{-1}	1.124×10^{-2}	2.154×10^{-3}
	$\dot{\omega}$	1.534×10^{-2}	-6.496×10^{-3}	2.843×10^{-3}
	$\ddot{\omega}$	2.792×10^{-4}	-3.190×10^{-4}	-8.332×10^{-5}
(3,1)	A	5.358×10^{-3}	2.113×10^{-3}	1.367×10^{-3}
	$\dot{A}$	2.413×10^{-4}	5.772×10^{-5}	5.734×10^{-5}
	$\ddot{A}$	4.851×10^{-6}	7.180×10^{-5}	6.059×10^{-6}
	ω	4.189×10^{-1}	7.247×10^{-2}	-2.821×10^{-2}
	$\dot{\omega}$	-2.106×10^{-3}	-1.196×10^{-2}	7.362×10^{-3}
	$\ddot{\omega}$	-1.256×10^{-2}	-1.138×10^{-2}	1.408×10^{-3}

TABLE VIII. Global fits of the coefficients for the quantities used to determine NQC corrections for $t^{\rm NQC}_{\ell m} = t^{\rm peak}_{A_{\ell m}} - 2$. The fitting template is a quadratic function: $y = C_{\rm QC} + C_1 \hat{b}_{\Omega_{\rm pk}} + C_2 \hat{b}^2_{\Omega_{\rm pk}}$. The amplitude considered in this table is RWZ-normalized as usual, i.e. $A_{\ell m} = |\Psi_{\ell m}| = |h_{\ell m}|/\sqrt{(\ell+2)(\ell+1)\ell(\ell-1)}$.

(ℓ, m)	$X^{\rm NQC}_{\ell m}$	$C_{\rm QC}$	C_1	C_2
(4,4)	A	1.440×10^{-2}	1.261×10^{-2}	1.215×10^{-2}
	$\dot{A}$	1.124×10^{-4}	-1.072×10^{-4}	-3.334×10^{-5}
	$\ddot{A}$	-4.584×10^{-5}	5.504×10^{-5}	1.442×10^{-6}
	ω	6.041×10^{-1}	4.204×10^{-2}	1.016×10^{-3}
	$\dot{\omega}$	1.476×10^{-2}	-1.500×10^{-2}	-1.774×10^{-4}
	$\ddot{\omega}$	3.536×10^{-4}	1.146×10^{-3}	-1.417×10^{-3}
(4,3)	A	4.887×10^{-3}	3.881×10^{-3}	3.445×10^{-3}
	$\dot{A}$	7.313×10^{-5}	-3.014×10^{-6}	5.836×10^{-6}
	$\ddot{A}$	-3.104×10^{-5}	5.333×10^{-6}	-3.956×10^{-6}
	ω	5.980×10^{-1}	1.029×10^{-2}	-1.114×10^{-2}
	$\dot{\omega}$	1.979×10^{-2}	-7.181×10^{-3}	-3.824×10^{-4}
	$\ddot{\omega}$	-1.791×10^{-4}	1.279×10^{-3}	3.702×10^{-4}
(4,2)	A	1.627×10^{-3}	8.138×10^{-4}	5.752×10^{-4}
	$\dot{A}$	2.687×10^{-5}	7.489×10^{-6}	4.104×10^{-5}
	$\ddot{A}$	-1.470×10^{-5}	-1.090×10^{-5}	-7.254×10^{-6}
	ω	5.784×10^{-1}	2.331×10^{-2}	-2.894×10^{-2}
	$\dot{\omega}$	2.622×10^{-2}	-4.593×10^{-3}	-3.936×10^{-3}
	$\ddot{\omega}$	-4.671×10^{-4}	6.784×10^{-3}	-4.209×10^{-3}
(4,1)	A	4.311×10^{-4}	1.636×10^{-4}	1.081×10^{-4}
	$\dot{A}$	4.004×10^{-5}	7.867×10^{-6}	1.042×10^{-5}
	$\ddot{A}$	5.997×10^{-6}	1.533×10^{-5}	9.482×10^{-8}
	ω	5.673×10^{-1}	9.191×10^{-2}	-3.606×10^{-2}
	$\dot{\omega}$	-1.560×10^{-2}	-1.071×10^{-2}	8.617×10^{-3}
	$\ddot{\omega}$	-3.018×10^{-2}	-3.355×10^{-2}	5.444×10^{-3}
(5,5)	A	5.151×10^{-3}	5.057×10^{-3}	5.331×10^{-3}
	$\dot{A}$	5.170×10^{-5}	-2.949×10^{-5}	-2.260×10^{-5}
	$\ddot{A}$	-2.150×10^{-5}	1.723×10^{-5}	6.342×10^{-6}
	ω	7.789×10^{-1}	4.215×10^{-2}	6.786×10^{-4}
	$\dot{\omega}$	1.894×10^{-2}	-1.663×10^{-2}	-1.112×10^{-3}
	$\ddot{\omega}$	2.169×10^{-4}	1.746×10^{-3}	-1.577×10^{-3}

[1] B. P. Abbott *et al.* (LIGO Scientific and Virgo Collaborations), Phys. Rev. Lett. **116**, 061102 (2016).

[2] B. P. Abbott *et al.* (LIGO Scientific and Virgo Collaborations), Phys. Rev. X **9**, 031040 (2019).

[3] R. Abbott *et al.* (LIGO Scientific and Virgo Collaborations), Phys. Rev. X **11**, 021053 (2021).

[4] R. Abbott *et al.* (LIGO Scientific, Virgo, and KAGRA Collaborations), Report No. LIGO-P2000318, arXiv:2111.03606.

[5] R. Gamba, M. Breschi, G. Carullo, P. Rettegno, S. Albanesi, S. Bernuzzi, and A. Nagar, Nat. Astron. **7**, 11 (2023).

[6] A. Bonino, R. Gamba, P. Schmidt, A. Nagar, G. Pratten, M. Breschi, P. Rettegno, and S. Bernuzzi, Phys. Rev. D **107**, 064024 (2023).

[7] A. Buonanno and T. Damour, Phys. Rev. D **59**, 084006 (1999).

[8] A. Buonanno and T. Damour, Phys. Rev. D **62**, 064015 (2000).

[9] T. Damour, P. Jaranowski, and G. Schaefer, Phys. Rev. D **62**, 084011 (2000).
[10] T. Damour, Phys. Rev. D **64**, 124013 (2001).
[11] T. Damour, P. Jaranowski, and G. Schäfer, Phys. Rev. D **91**, 084024 (2015).
[12] A. Buonanno, G. B. Cook, and F. Pretorius, Phys. Rev. D **75**, 124018 (2007).
[13] T. Damour and A. Nagar, Phys. Rev. D **76**, 064028 (2007).
[14] F. Pretorius, Phys. Rev. Lett. **95**, 121101 (2005).
[15] A. Nagar, T. Damour, and A. Tartaglia, Classical Quantum Gravity **24**, S109 (2007).
[16] S. Bernuzzi and A. Nagar, Phys. Rev. D **81**, 084056 (2010).
[17] S. Bernuzzi, A. Nagar, and A. Zenginoglu, Phys. Rev. D **83**, 064010 (2011).
[18] N. Yunes, A. Buonanno, S. A. Hughes, Y. Pan, E. Barausse, M. Coleman Miller, and W. Throwe, Phys. Rev. D **83**, 044044 (2011).
[19] E. Barausse, A. Buonanno, S. A. Hughes, G. Khanna, S. O'Sullivan, and Y. Pan, Phys. Rev. D **85**, 024046 (2012).
[20] S. Albanesi, A. Nagar, and S. Bernuzzi, Phys. Rev. D **104**, 024067 (2021).
[21] P. Amaro-Seoane *et al.* (LISA Collaboration), arXiv:1702.00786.
[22] S. Babak, J. Gair, A. Sesana, E. Barausse, C. F. Sopuerta, C. P. L. Berry, E. Berti, P. Amaro-Seoane, A. Petiteau, and A. Klein, Phys. Rev. D **95**, 103012 (2017).
[23] C. P. L. Berry, S. A. Hughes, C. F. Sopuerta, A. J. K. Chua, A. Heffernan, K. Holley-Bockelmann, D. P. Mihaylov, M. C. Miller, and A. Sesana, arXiv:1903.03686.
[24] A. Pound, Fund. Theor. Phys. **179**, 399 (2015).
[25] L. Barack and A. Pound, Rep. Prog. Phys. **82**, 016904 (2019).
[26] N. Warburton, A. Pound, B. Wardell, J. Miller, and L. Durkan, Phys. Rev. Lett. **127**, 151102 (2021).
[27] M. Van De Meent and N. Warburton, Classical Quantum Gravity **35**, 144003 (2018).
[28] A. Albertini, A. Nagar, A. Pound, N. Warburton, B. Wardell, L. Durkan, and J. Miller, Phys. Rev. D **106**, 084061 (2022).
[29] A. Albertini, A. Nagar, A. Pound, N. Warburton, B. Wardell, L. Durkan, and J. Miller, Phys. Rev. D **106**, 084062 (2022).
[30] T. Damour, Phys. Rev. D **81**, 024017 (2010).
[31] L. Barack, T. Damour, and N. Sago, Phys. Rev. D **82**, 084036 (2010).
[32] A. Le Tiec, E. Barausse, and A. Buonanno, Phys. Rev. Lett. **108**, 131103 (2012).
[33] E. Barausse, A. Buonanno, and A. Le Tiec, Phys. Rev. D **85**, 064010 (2012).
[34] A. Antonelli, M. van de Meent, A. Buonanno, J. Steinhoff, and J. Vines, Phys. Rev. D **101**, 024024 (2020).
[35] A. Nagar and S. Albanesi, Phys. Rev. D **106**, 064049 (2022).
[36] T. Regge and J. A. Wheeler, Phys. Rev. **108**, 1063 (1957).
[37] F. J. Zerilli, Phys. Rev. Lett. **24**, 737 (1970).
[38] A. Nagar and L. Rezzolla, Classical Quantum Gravity **22**, R167 (2005).
[39] K. Martel and E. Poisson, Phys. Rev. D **71**, 104003 (2005).
[40] S. Bernuzzi, A. Nagar, and A. Zenginoglu, Phys. Rev. D **84**, 084026 (2011).
[41] S. Bernuzzi, A. Nagar, and A. Zenginoglu, Phys. Rev. D **86**, 104038 (2012).
[42] T. Damour and A. Nagar, Phys. Rev. D **90**, 024054 (2014).
[43] D. Chiaramello and A. Nagar, Phys. Rev. D **101**, 101501 (2020).
[44] K. Martel, Phys. Rev. D **69**, 044025 (2004).
[45] V. Baibhav, M. H.-Y. Cheung, E. Berti, V. Cardoso, G. Carullo, R. Cotesta, W. Del Pozzo, and F. Duque, arXiv:2302.03050.
[46] T. Damour, B. R. Iyer, and A. Nagar, Phys. Rev. D **79**, 064004 (2009).
[47] M. Khalil, A. Buonanno, J. Steinhoff, and J. Vines, Phys. Rev. D **104**, 024046 (2021).
[48] A. Placidi, S. Albanesi, A. Nagar, M. Orselli, S. Bernuzzi, and G. Grignani, Phys. Rev. D **105**, 104030 (2022).
[49] S. Albanesi, A. Placidi, A. Nagar, M. Orselli, and S. Bernuzzi, Phys. Rev. D **105**, L121503 (2022).
[50] G. Riemenschneider, P. Rettegno, M. Breschi, A. Albertini, R. Gamba, S. Bernuzzi, and A. Nagar, Phys. Rev. D **104**, 104045 (2021).
[51] A. Nagar, P. Rettegno, R. Gamba, A. Albertini, and S. Bernuzzi, arXiv:2304.09662.
[52] T. Damour, A. Nagar, and S. Bernuzzi, Phys. Rev. D **87**, 084035 (2013).
[53] R. Cotesta, A. Buonanno, A. Bohé, A. Taracchini, I. Hinder, and S. Ossokine, Phys. Rev. D **98**, 084028 (2018).
[54] S. Ossokine *et al.*, Phys. Rev. D **102**, 044055 (2020).
[55] L. Pompili *et al.*, arXiv:2303.18039.
[56] A. Ramos-Buades, A. Buonanno, H. Estellés, M. Khalil, D. P. Mihaylov, S. Ossokine, L. Pompili, and M. Shiferaw, arXiv:2303.18046.
[57] E. Harms, S. Bernuzzi, A. Nagar, and A. Zenginoğlu, Classical Quantum Gravity **31**, 245004 (2014).
[58] A. Taracchini, A. Buonanno, G. Khanna, and S. A. Hughes, Phys. Rev. D **90**, 084025 (2014).
[59] T. Damour and A. Nagar, Phys. Rev. D **79**, 081503 (2009).
[60] E. W. Leaver, Phys. Rev. D **34**, 384 (1986).
[61] N. Andersson, Phys. Rev. D **55**, 468 (1997).
[62] A. Zenginoğlu, Classical Quantum Gravity **27**, 045015 (2010).
[63] J. L. Lagrange, Oeuvres de Lagrange **6**, 713 (1808).
[64] J. L. Lagrange, Oeuvres de Lagrange **6**, 771 (1809).
[65] J. L. Lagrange, Oeuvres de Lagrange **6**, 809 (1810).
[66] A. Nagar, P. Rettegno, R. Gamba, and S. Bernuzzi, Phys. Rev. D **103**, 064013 (2021).
[67] A. Nagar, A. Bonino, and P. Rettegno, Phys. Rev. D **103**, 104021 (2021).
[68] A. V. Joshi, S. G. Rosofsky, R. Haas, and E. A. Huerta, Phys. Rev. D **107**, 064038 (2023).
[69] I. M. Romero-Shaw, D. Gerosa, and N. Loutrel, Mon. Not. R. Astron. Soc. **519**, 5352 (2023).
[70] M. A. Shaikh, V. Varma, H. P. Pfeiffer, A. Ramos-Buades, and M. van de Meent, arXiv:2302.11257.
[71] T. Damour, A. Nagar, E. N. Dorband, D. Pollney, and L. Rezzolla, Phys. Rev. D **77**, 084017 (2008).
[72] T. Damour, A. Nagar, M. Hannam, S. Husa, and B. Brügmann, Phys. Rev. D **78**, 044039 (2008).